REVIEW

Advanced Diffusion-Weighted MRI for Cancer Microstructure Assessment in Body Imaging, and Its Relationship With Histology

Ella Fokkinga, MSc,[1,2] Juan A. Hernandez-Tamames, PhD,[3,4] Andrada Ianus, PhD,[5] Markus Nilsson, PhD,[6] Chantal M. W. Tax, PhD,[7,8] Raquel Perez-Lopez, MD, PhD,[2*] and Francesco Grussu, PhD[2*]

Diffusion-weighted magnetic resonance imaging (DW-MRI) aims to disentangle multiple biological signal sources in each imaging voxel, enabling the computation of innovative maps of tissue microstructure. DW-MRI model development has been dominated by brain applications. More recently, advanced methods with high fidelity to histology are gaining momentum in other contexts, for example, in oncological applications of body imaging, where new biomarkers are urgently needed. The objective of this article is to review the state-of-the-art of DW-MRI in body imaging (ie, not including the nervous system) in oncology, and to analyze its value as compared to reference colocalized histology measurements, given that demonstrating the histological validity of any new DW-MRI method is essential. In this article, we review the current landscape of DW-MRI techniques that extend standard apparent diffusion coefficient (ADC), describing their acquisition protocols, signal models, fitting settings, microstructural parameters, and relationship with histology. Preclinical, clinical, and in/ex vivo studies were included. The most used techniques were intravoxel incoherent motion (IVIM; 36.3% of used techniques), diffusion kurtosis imaging (DKI; 16.7%), vascular, extracellular, and restricted diffusion for cytometry in tumors (VERDICT; 13.3%), and imaging microstructural parameters using limited spectrally edited diffusion (IMPULSED; 11.7%). Another notable category of techniques relates to innovative *b*-tensor diffusion encoding or joint diffusion-relaxometry. The reviewed approaches provide histologically meaningful indices of cancer microstructure (eg, vascularization/cellularity) which, while not necessarily accurate numerically, may still provide useful sensitivity to microscopic pathological processes. Future work of the community should focus on improving the inter-/intra-scanner robustness, and on assessing histological validity in broader contexts.
Level of Evidence: NA
Technical Efficacy: Stage 2

J. MAGN. RESON. IMAGING 2023.

Diffusion-weighted (DW) magnetic resonance imaging (MRI) detects signals that encode water diffusion in the body. Its ultimate goal is the estimation of the tissue *microstructure* that determines diffusion patterns, that is, statistics of biological properties at the ~1–100 μm length scale, from sets of MRI signal measurements.[1,2] Motion-probing gradients are used to encode salient characteristics of water diffusion in tissues into the MRI signal. The classical

View this article online at wileyonlinelibrary.com. DOI: 10.1002/jmri.29144

Received Aug 11, 2023, Accepted for publication Oct 31, 2023.

*Address reprint requests to: R.P.-L., Cellex Center, Carrer de Natzaret 115-117, 08035 Barcelona, Spain. E-mail: rperez@vhio.net, or F.G., Cellex Center, Carrer de Natzaret 115-117, 08035 Barcelona, Spain. E-mail: fgrussu@vhio.net
R.P.-L. and F.G. are the joint last (senior) authors.

From the [1]Biomedical Engineering, Track Medical Physics, Delft University of Technology, Delft, The Netherlands; [2]Radiomics Group, Vall d'Hebron Institute of Oncology, Vall d'Hebron Barcelona Hospital Campus, Barcelona, Spain; [3]Department of Radiology and Nuclear Medicine, Erasmus MC, Rotterdam, The Netherlands; [4]Department of Imaging Physics, Delft University of Technology, Delft, The Netherlands; [5]Champalimaud Research, Champalimaud Foundation, Lisbon, Portugal; [6]Department of Diagnostic Radiology, Clinical Sciences Lund, Lund, Sweden; [7]Cardiff University Brain Research Imaging Center (CUBRIC), School of Physics and Astronomy, Cardiff University, Cardiff, United Kingdom; and [8]Image Sciences Institute, University Medical Center Utrecht, Utrecht, The Netherlands

Additional supporting information may be found in the online version of this article

DW-MRI experiment is based on the pulsed gradient spin echo (PGSE) sequence, also known as the Stejskal-Tanner experiment,[3] Single diffusion encoding, or linear tensor encoding (LTE).[4] The idealized PGSE experiment is illustrated in Fig. 1, in which motion-probing magnetic field gradients are placed on either side of a spin echo refocusing pulse. Several approaches have been proposed to enable microstructure estimation, and the latest methods entail rich acquisitions coupled with sophisticated signal modeling (Appendix A).

A number of recent articles have reviewed the state-of-the-art of DW-MRI applications.[5–8] However, these tend to focus heavily on brain imaging, especially in neurological or psychiatric disorders, while reviews in the context of other areas as body imaging in oncology are limited,[9–11] despite the rapidly growing amount of research in this field. Moreover, while DW-MRI is intimately related to histology, recent reviews do not typically assess the techniques taking into account their actual histological validity and histopathological specificity. Histological validation is a key step in the development of any new DW-MRI approach, as it is essential to assess the implications of the modeling assumptions, and to confirm that the method is actually sensitive and specific to the histopathological characteristics that it intends to measure.[2]

Given the importance of linking DW-MRI measures with the underlying tissue histology, the objective of this paper is to review the state-of-the-art of DW-MRI in the context of oncological body imaging (beyond the central nervous system, ie, mainly abdominal and pelvic imaging), with an emphasis on their value in the assessment of microstructure as compared to reference histopathology. We specifically aimed to provide an overview of the landscape of advanced DW-MRI methods that extend apparent diffusion coefficient (ADC), focusing on techniques whose indices have been compared to histology in oncological body imaging. In doing so, we took a mainly narrative approach, while also presenting some quantitative information from the articles. This was related to the application area (anatomical, cancer type), scanning settings, and level of correlation histology.

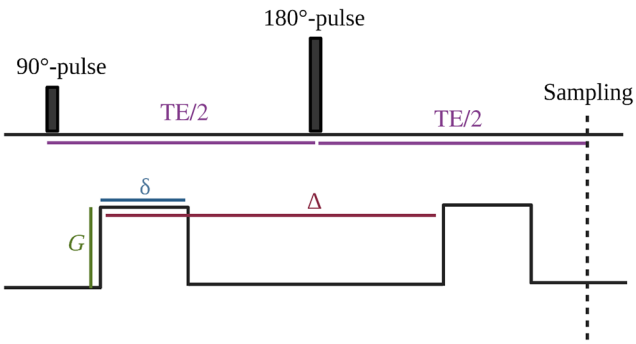

FIGURE 1: Schematic of the idealized pulsed-gradient spin-echo (PGSE) sequence. The first and second radiofrequency (RF) pulses rotate the magnetization vector by 90° and 180°, respectively. These two pulses are characteristic for a spin-echo sequence, as they consecutively excite and refocus the magnetization. After a time TE (the echo time), a spin echo is formed and the center of the k-space is sampled. The diffusion encoding gradient consists of two pulsed wave forms on each side of the 180°, which diffusion-weight the spin echo. The diffusion gradient is characterized by a gradient magnitude *G*, the gradient duration *δ*, and the separation time in between the two gradient lobes Δ. Note that the figure represents a simplified theoretical schematic of PGSE. In real world, the gradient pulses are not rectangular but rather trapezoidal, due to technical requirements.

Methods

DW-MRI Technique Selection

Given the high number of DW-MRI methods used to assess microstructure and the variety of approaches followed to relate DW-MRI and histology, we carried out a literature search in PubMed to guide the selection of the techniques in this review. The search aimed to identify techniques that are relevant to body imaging, and that offer sensitivity to the underlying tissue histology (search query: Appendix B). The search adhered to the Preferred Items for Systematic Reviews and Meta-analyses Extension for Scoping Reviews (PRISMA-ScR) guidelines[12] and was performed on September 8, 2023.

Inclusion criteria were: 1) primary study; 2) English language; 3) report an application of DW-MRI; 4) the DW-MRI technique provides a direct estimate of a microstructural property, or offers some markers that extend routine ADC (so that they rely on a signal model with more tissue parameters than simple ADC mapping); 4) focused on preclinical, clinical, in/ex vivo oncology studies (studies that compared DW-MRI metrics from animal or human cancer cells or tissue, scanned either in vivo or ex vivo, and then compared to metrics derived from microscopy performed on the same specimens after MRI); 5) focused on body imaging (ie, on applications that do not include imaging of the nervous system).

Technique Application and MRI-Histology Correlation Assessments

We screened all included articles and recorded the MRI scanner used, the tissue condition during MR imaging, the area of application, as well as correlation coefficients between any DW-MRI and histological metric, whenever reported.

Narrative Description of the Selected Techniques

For each identified technique, we described 1) signal model or representation, 2) required diffusion encoding protocol, 3) fitting methods, 4) main histological correlates, and finally 5) discussed its strengths and weaknesses. Note that with both signal "model" and "representation" we mean a functional form capable of predicting the diffusion MRI signal for a variety of

possible diffusion protocols given a set of tissue parameters. These can be inferred through fitting to sets of DW-MRI signal measurements. In the case of models, these parameters typically refer to histological characteristics, such as cell size or cell density. Tissue parameters in signal representations instead are apparent phenomenological properties that are sensitive to different histological characteristics at once, and typically change when the diffusion encoding gradient timings vary (eg, apparent diffusion coefficient or kurtosis).

Results

DW-MRI Technique Selection

A total of 354 articles were identified. 87 articles were excluded based on title and abstract. Of the remaining 267 articles, 238 focused on the use of techniques that compute indirect measures of microstructure and 29 focused on techniques that provide direct estimates of histological properties. Of 238 articles, 213 were excluded as they either did not report any comparison to histology, or, if they did, only for ADC. Of 267 articles, 54 were finally included in this review. Figure 2 graphically summarizes the article screening process.

The following techniques were identified: diffusion kurtosis imaging (DKI); intravoxel incoherent motion (IVIM) imaging; vascular, extracellular, and restricted diffusion for cytometry in tumors (VERDICT); imaging microstructural parameters using limited spectrally edited diffusion (IMPULSED); stretched exponential model (SEM); q-space imaging (QSI); MRI-cytometry; restriction spectrum imaging (RSI); Monte Carlo (MC) simulations for microstructural mapping from clinical DW-MRI; multidimensional diffusion MRI (MDD-MRI); hybrid multidimensional MRI (HM-MRI); diffusion-relaxation correlation spectrum imaging (DR-CSI); and mpMRI-based artificial intelligence (AI). Some articles focused on more than one technique.

A summary of the included techniques is given in Table 1 and Fig. 3. Techniques are grouped as phenomenological, when they parametrize the signal to surrogate parameters that do have a direct microstructural counterpart (eg, diffusion kurtosis), or biophysical models, if they estimate specific histology features (eg, cell size).

Technique Application and MRI-Histology Correlation Assessments

Supporting Information Tables S1–S7 report in detail information on the MRI scanner and DW protocol, tissue condition during MR imaging, area of application, and

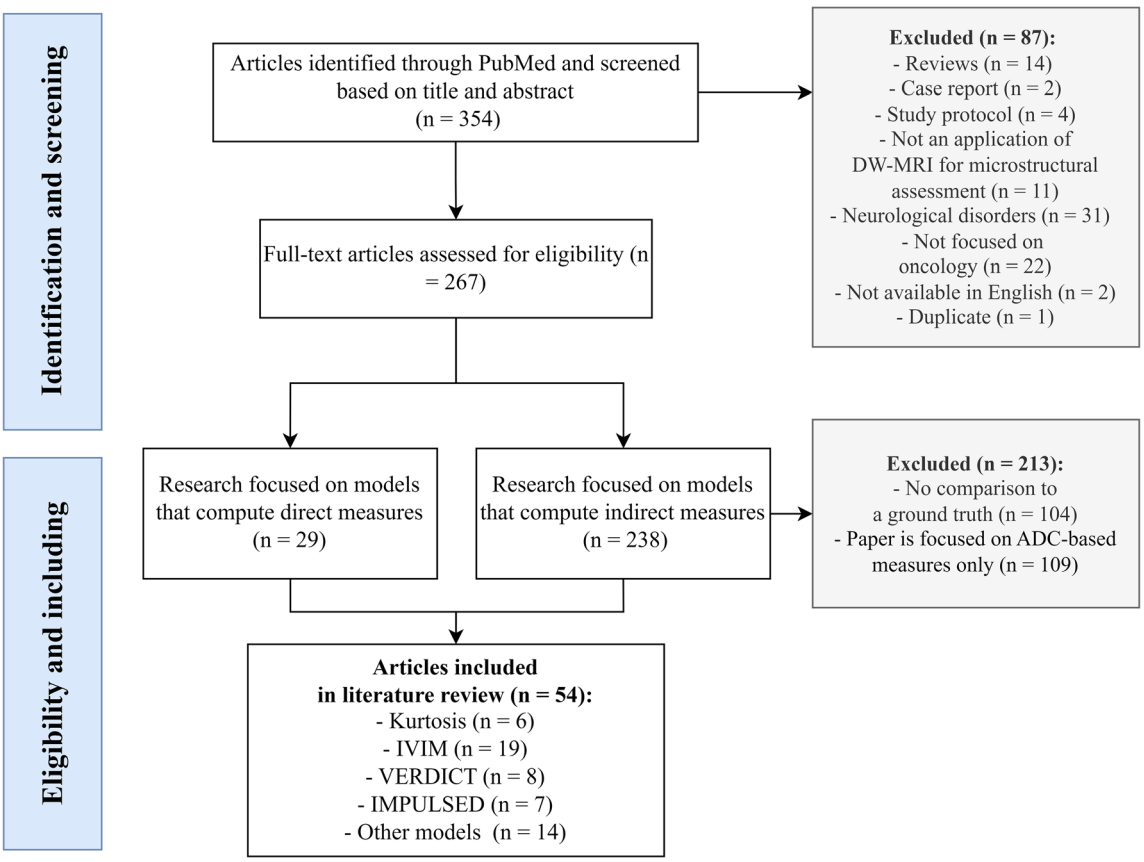

FIGURE 2: Flow chart of the literature search in PubMed. Acronyms stand for: DW = diffusion-weighted; IVIM = intravoxel incoherent motion; VERDICT = vascular, extracellular, and restricted diffusion for cytometry in tumors; IMPULSED = imaging microstructural parameters using limited spectrally edited diffusion.

TABLE 1. Summary of the Diffusion Models and Signal Representations Included in this review.

Model/ Representation	Reported by	Model Parameters	Salient MR-Acquisition Protocol Requirements	Main Histological Correlates Assessed
DKI	13–19	ADC_k, K	High b-values required to sample non-Gaussian diffusion	Cellularity
IVIM	20,21,26–43	D_t, D^*, f	Many b-values required, including low b-values to sample pseudo-diffusion	Cellularity, vessel density measures
VERDICT	52–59	*cell radius R*, f_{ic}, f_{EES}, f_{vasc}, d_{ic}, d_{ec}, d_{vasc}	PGSE protocol probing various different TE, gradient duration, and separations. Novel non-PGSE encodings recently explored	Cellularity, intracellular fraction, cell size
IMPULSED	63–69	*cell radius R*, f_{ic}, d_{ic}, d_{ec}	Uses OGSE in addition to PGSE	Cellularity, intracellular fraction, cell size
SEM	17,33,71	D_{SEM}, α	PGSE protocol probing different low and intermediate b-values at fixed diffusion time	Cellularity, heterogeneity
QSI	71,73	Statistics from spin displacement distribution profiles	PGSE protocol probing different q-values required, with high gradient strength required	Cellularity, nuclear-to-cytoplasm ratio
MRI-Cytometry	78	Probability distribution of cell size radius R, d_{ic}, d_{ec}, f_{ic}, extracellular DTD factor β	General framework, so can be applied for multiple acquisition protocols	Cell size
RSI	22,79	Volume fractions C_n	PGSE with high b-values required, but relatively short scan time (it can be performed at fixed diffusion time)	Indices of intravoxel tissue composition
MDD-MRI	85	Statistical descriptors of diffusion tensor distributions	Uses a variety of anisotropic or isotropic b-tensor encodings; for example, gradient waveforms implementing isotropic linear encoding along multiple directions as well as spherical tensor encoding	Indices of tissue composition
HM-MRI	91,92	The volume fractions V_n, the T_{2n}, and the ADC_n-value for the lumen, stroma, and epithelium	Part of an mp-MRI protocol including T2-weighted, DCE, and diffusion imaging (PGSE at varying b-values and TE, with no requirements on diffusion time)	Indices of tissue composition

TABLE 1. Continued

Model/ Representation	Reported by	Model Parameters	Salient MR-Acquisition Protocol Requirements	Main Histological Correlates Assessed
DR-CSI	99,100	Volume fractions f_n	Part of an mp-MRI protocol including T2-weighted and diffusion imaging (PGSE at varying b-values and TE, with no requirements on diffusion time)	Indices of tissue composition
MC DW-MRI	81	Cell radius and vol. fraction R and f_{ic}, cell diffusivity d_{ic} and apparent cellularity ρ_{app}	Part of a clinical mp-MRI protocol including anatomical MRI and clinical DW-MRI for ADC mapping (no requirements on diffusion time)	Ki-67 expression
mpMRI-based AI	101	Cellularity	Part of an mp-MRI protocol including T2-weighted, DCE, and simple ADC mapping based on PGSE	Cellularity

Model abbreviations: DKI = diffusion kurtosis imaging; IVIM = intravoxel incoherent motion; VERDICT = vascular, extracellular, and restricted diffusion for cytometry in tumors; IMPULSED = imaging microstructural parameters using limited spectrally edited diffusion; SEM = stretched exponential model; QSI = q-space imaging; RSI = restricted spectrum imaging; MDD-MRI = multidimensional diffusion MRI; HM-MRI = hybrid multidimensional MRI; DR-CSI = diffusion-relaxation correlation spectrum imaging; mpMRI = multiparametric MRI; MC DW-MRI = Monte Carlo simulations for microstructural mapping from clinical DW-MRI; AI = artificial intelligence.

information on the correlation of MRI metrics to histology for all 54 articles. This information is also included as a structured CSV dataset in Supporting Information Data S2.

Figure 4 graphically visualizes information on the MRI-histology applications extracted from the selected articles. The figure shows that in most studies (about 60%), 3 T MRI scanners were used (Fig. 4a). Human tissue was used in 60% of cases, followed by mouse tissue in almost 30% of the experiments (Fig. 4b). In the vast majority of the experiments (roughly 80%), tissues were imaged in vivo, while ex vivo imaging (of either fresh or fixed tissue) was performed in 13% of the experiments (Fig. 4c). Finally, the analysis of the included articles reveals that the cancer application that were investigated varied considerably (Fig. 4d). The three most common areas of interest were, in decreasing order, cancers of the prostate (23% of the experiments), breast (16.4% of the experiments), and liver (14.8% of the experiments).

Tables 2 and 3 report correlation coefficients between DW-MRI metrics and histology (Table 2: DKI and IVIM metrics; Table 3: all other techniques). Correlations vary from weak (eg, $r = 0.22$ for SEM parameter α with nuclear-to-cytoplasm ratio) to strong (eg, $r = 0.92$ for IMPULSED cell diameter d with histology-derived cell size). Moreover, for some metrics correlations not always consistent across studies (eg, $r = 0.78$ and $r = -0.41$ for IVIM D^* and microvessel density), while for others they are (eg, DKI ADC_K or SEM D_t are consistently negatively correlated with metrics of cellularity or cell count). Promisingly high correlations are, for example, those observed in prostate cancer for diffusion-relaxation methods (r of 0.67 and 0.90 between MRI and histological prostate lumen fraction).

Narrative Description of the Selected Techniques

This section describes the advanced DW-MRI techniques that were used in the 54 articles included in this review, discussing the key metrics that each technique provides.

DIFFUSION KURTOSIS IMAGING. Ten articles report on DKI[13–22] (Supporting Information Table S1 for all but articles[20–22], which are reported in Supporting Information Table S2[20,21] and S5,[22] being focused on more than one DW-MRI technique). DKI is a technique based on the diffusion signal cumulant expansion,[23] and was proposed by Jensen et al in 2005 to characterize non-Gaussian diffusion arising from presence of multiple water pools with different

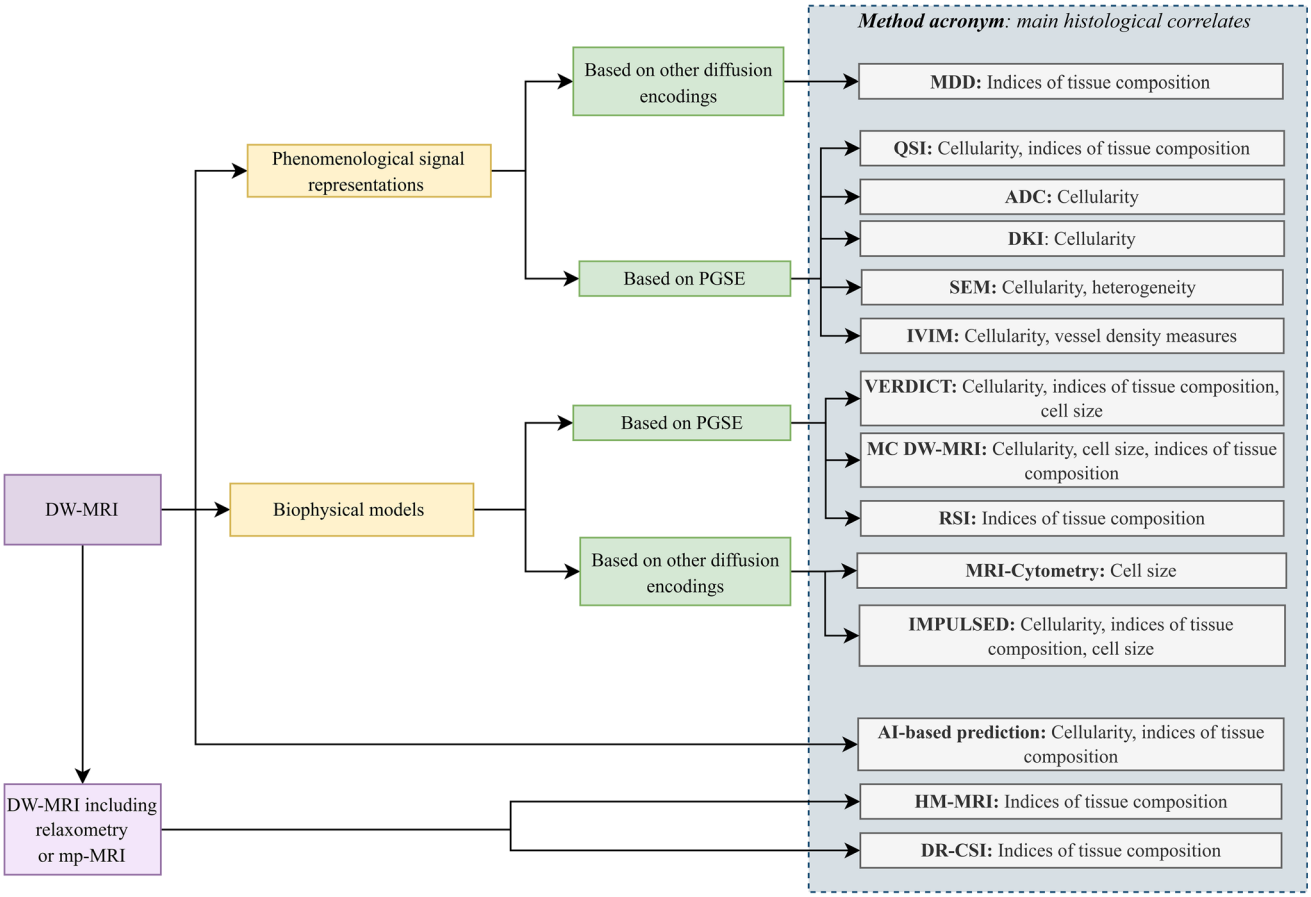

FIGURE 3: A visual summary of the techniques found in the literature search and their main histological correlates. PGSE = pulsed gradient spin echo; DKI = diffusion kurtosis imaging; IVIM = intravoxel incoherent motion; VERDICT = vascular, extracellular, and restricted diffusion for cytometry in tumors; IMPULSED = imaging microstructural parameters using limited spectrally edited diffusion; SEM = stretched exponential modeling; QSI = q-space imaging; RSI = restricted spectrum imaging; MDD-MRI = multidimensional diffusion MRI; HM-MRI = hybrid multidimensional MRI; DR-CSI = diffusion-relaxation correlation spectrum imaging; MC DW-MRI = Monte Carlo simulations for microstructural mapping from clinical DW; mpMRI = multiparametric MRI; AI = artificial intelligence.

diffusivities, restriction, water exchange, or combination of those.[24]

Signal model: The DKI signal representation is

$$S = S_0 \exp\left(-b\,\mathrm{ADC}_k + \frac{1}{6}K\,(b\,\mathrm{ADC}_k)^2\right) \qquad (1)$$

Above, S is the signal and b is the b-value. Unknown parameters are the non-DW signal level S_0, an ADC metric ADC_k, the excess kurtosis K ($K = 0$ for Gaussian diffusion), and the non-DW-signal S_0. ADC_k is a corrected estimate of ADC as compared to a first-order description $S = S_0 \exp(-b\mathrm{ADC})$ (for sufficiently low b-values, $\mathrm{ADC}_k \approx \mathrm{ADC}$, $K \approx 0$). K is unitless; the larger $|K|$, the stronger the departure from Gaussian diffusion (ie, from mono-exponential signal decay). Negative K is possible, but rarely measured. In some articles, a full tensor fit is performed, and Eq. 1 is generalized to account for anisotropy in apparent diffusivity and apparent kurtosis across three-dimensional (3D) spatial directions.[18,19] In those cases, the authors typically focused their analyses on mean diffusivity and mean kurtosis, which here were then taken as proxies for ADC_k and K in Table 2.

Required diffusion encoding protocol: Clinical DKI is based on PGSE (ie, LTE), with 3 mutually orthogonal gradient directions at b-values up to approximately 1000–2000 seconds/mm^2. The measurement regime where estimating K becomes relevant depends on the microstructure. Typically, K cannot be neglected when the estimated ADC starts to become dependent on the maximum b-value. Signals from the three directions are averaged (either geometrically or arithmetically) and scalar kurtosis evaluated, rather than full tensors (required in tissues such as muscles and white matter), due to low anisotropy. To estimate S_0, ADC_k and K, sampling at least three b-values up to 1000–2000 seconds/mm^2 is required.

Fitting methods: The included articles used voxel-wise, nonlinear least-squares fitting, which were implemented in MATLAB.[13,14]

Main histological correlates: DKI-parameters are not direct estimates of microstructural properties as cell size/density. Nonetheless, they are sensitive to several different

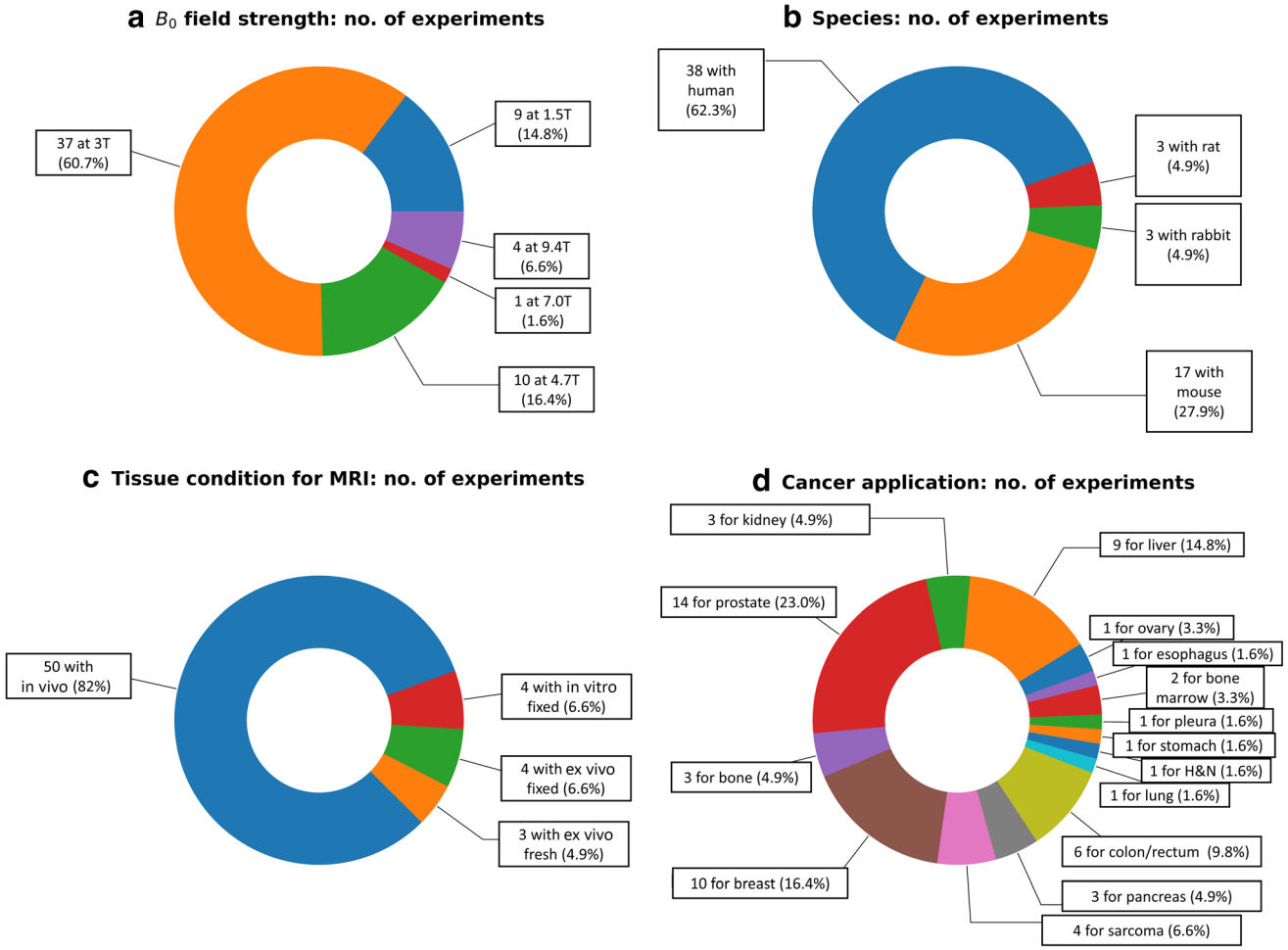

FIGURE 4: Salient statistics regarding the MRI-histology experiments performed in the identified articles. (a) B_0 magnetic field strength used for MRI. (b) Species from which the imaged tissues were obtained. (c) Tissue condition during MRI. (d) Main cancer application.

biophysical characteristics, and can serve as indirect markers of microstructure. In four articles, K or full tensorial mean kurtosis were tested for correlation to cellularity,[13,14,18,19] with mixed results. In a study on ovarian cancer,[13] cellularity correlated with K; in hepatocellular carcinoma (HCC)[14] and in a rabbit VX2 bone tumor model,[18] it did not. Since K reflects diffusional heterogeneity, it is possible that such variable correlations with cellularity reflect, at least in part, intravoxel heterogeneity in cell density.[25] Intracellular fraction from histology and other tissue component fractions were compared to K in renal cell carcinoma and prostate,[16,17] and results varied (correlation not always seen).

ADC_K or full tensorial mean diffusivity exhibited similar correlations as K with cellularity, but inverse. It was found to have a significant inverse correlation with cellularity,[13,18,19] and tissue composition fractions.[16,17] Combining ADC_k and K resulted in an even stronger correlation to cytoplasm, cellular, and stromal fraction.[17]

Rosenkrantz et al[14] found weak correlations among ADC, ADC_k, and K, implying that K may offer complementary information, even if fully biologically specific. This is supported by the fact that non-Gaussian diffusion was seen in all HCC cases ($K > 0.5$). K exhibited a higher coefficient of variation (CV) than ADC, reflecting higher sensitivity to diffusion heterogeneity, but also potentially higher susceptibility to noise.

Grussu et al[15] mapped ADC_k and K to intracellular diffusivity and volume-weighted cell size at fixed diffusion time in fixed mouse livers. Cell size estimates were not accurate, but captured between-sample contrasts seen on histology.

Discussion: The main advance of DKI is that it provides additional information to routine ADC mapping accounting for non-Gaussian diffusion, which is quantified by the kurtosis excess K. DKI enables the description of a wider b-value range compared to ADC measurement, as it enables accounting for departures from mono-exponential signal decay. Nonetheless, DKI also has several limitations, and its practical implementation can be challenging. In order to accurately estimate the kurtosis, higher b-values than those typically acquired in the clinic are required, resulting in longer echo times and overall worse signal-to-noise ratio (SNR), as well as

TABLE 2. The Correlations Observed Between DKI and IVIM Metrics and Histological Indices Reported in the 54 Articles Included in This Review

MRI Metric	Correlation With Histology
DKI ADC_K	$r = -0.24$ with cellularity[14]; $r = -0.48$ with nuclear-to-cytoplasm ratio[16]; $r = -0.73$ (Spearman's) with cellularity[13]; $r = -0.77$, 0.63 with cellularity and apoptosis rate[18]; $r = -0.40$, -0.53, -0.55, 0.67 with nuclear, cytoplasmatic, cellular, and prostate stromal fractions[17]; $r = -0.83$, 0.72 with tumor cell density and CD45 level[19]; $r = 0.24$, -0.30 with stromal and nuclear fractions[20]; $r = -0.21$, 0.36 with tumor area and fraction of interstitium[21]; $r = -0.51$ (Spearman's) with tumor cellularity[71]
DKI K	$r = 0.48$ with cellularity[14]; $r = 0.54$ with nuclear-to-cytoplasm ratio[16]; $r = 0.49$, 0.53 (Spearman's) with cellularity and Ki-67 positive cell count[13]; $r = 0.28$, -0.23 with cellularity and apoptosis rate[18]; $r = 0.49$, 0.49, -0.42 with cytoplasmatic, cellular, and prostate stromal fractions[17]; $r = 0.35$, -0.24 with tumor cell density and CD45 level[19]; $r = -0.20$, 0.26, -0.29 with cellular, stromal, and nuclear fractions[20]; $r = 0.53$, 0.24, 0.38 with cancer cell nuclear area, lymphocyte area ratio, and cancer cell nucleus size[21]; $r = 0.28$ with tumor grade[22]
IVIM D_t	$r = -0.33$, -0.49, 0.42 with cell count, nuclear and stromal fractions[26]; $r = -0.46$ with percentage of fibrosis[30]; $r = -0.89$, -0.87, -0.84 with cell density, cell area fraction, and nuclear fraction[28]; $r = -0.39$ with tumor cellularity[27]; $r = -0.45$ (Spearman's) with nuclear-to-stromal ratio[31]; $r = -0.20$, 0.26, -0.29 with cellular, stromal, and nuclear fractions[20]; $r = -0.35$ with a fibrosis index[34]; $r = 0.52$, -0.20, 0.54 (Spearman's) with necrosis fraction, microvessel density, and apoptosis fraction[35]; $r = -0.47$, -0.50 (Spearman's) with microvessel density and area[37]; $r = 0.51$ with microvessel density[38]; $r = 0.84$ with necrotic fraction[39]; $r^2 = 0.46$ ($r = -0.68$) with cell density[40]; $r = -0.57$ with vasculogenic mimicry[41]; $r = -0.46$, -0.31 (Spearman's) with necrotic fraction and microvessel density[42]
IVIM D^*	$r = -0.26$ with percentage of fibrosis[30]; $r = 0.33$ with microvessel density[34]; $r = -0.38$, 0.54, -0.69 (Spearman's) with necrosis fraction, microvessel density and apoptosis fraction[35]; $r = 0.78$ (Spearman's) with microvessel density[36]; $r = -0.41$, -0.37 (Spearman's) with microvessel density and area[37]; $r = 0.71$, 0.72 with microvessel density and pericyte coverage index[41]; $r = 0.22$ with microvessel area fraction[21]; $r = 0.33$, 0.34 (Spearman's) with necrotic fraction and microvessel density[42]; $r = -0.92$, -0.79 with Ki-67-positive cell fraction and diameter[43]
IVIM f	$r = 0.35$, -0.42 with cell count and stromal fraction[26]; $r = 0.44$ with percentage of fibrosis[30]; $r = 0.63$, 0.61, 0.58 with endothelial area, total vessel area, microvessel count, and f entropy showed $r = -0.55$ with a Ki-67 index[29]; $r = -0.24$, 0.28, -0.24 with cellular, stromal, and nuclear fractions[20]; $r^2 = 0.40$ (ie, $r = 0.63$) with microvessel density[33]; $r = 0.42$ with a fibrosis index[34]; $r = -0.35$, 0.62, -0.55 (Spearman's) with necrosis fraction, microvessel density, and apoptosis fraction[35]; $r = 0.75$ (Spearman's) with microvessel density[36]; $r = 0.77$, 0.82 (Spearman's) with microvessel density and area[37]; $r = 0.28$ with microvessel density[38]; $r = 0.43$, 0.53 with microvessel density and necrotic fraction[39]; $r^2 = 0.44$ ($r = 0.66$) with blood vessel density[40]; $r = 0.52$, 0.38 with microvessel density and pericyte coverage index[41]; $r = 0.24$, 0.28, -0.37 with cancer cell area and nuclear fractions, lymphocyte area ratio[21]; $r = 0.40$, 0.44 (Spearman's) with necrotic fraction and microvessel density in mice injected with NCI-H226 cells, while $r = -0.51$, -0.55 in mice injected with MSTO-211H cells[42]; $r = -0.69$, -0.61 with Ki-67-positive cell fraction and diameter[43]

Weak correlations that in absolute value were lower than 0.2 were not included in the table. Values of r indicate Pearson's correlation coefficients, unless otherwise stated. Refer to section Advanced DW-MRI for the mathematical/physical foundations beyond each metric.

longer diffusion protocols, which may increase the sensitivity to motion. The higher requirements compared to ADC mapping are a limitation of virtually all advanced techniques described here, and will be given as understood when introducing the next techniques. Moreover, the estimation of the kurtosis can be ill-defined as ADC_k goes toward zero. Finally,

TABLE 3. The Correlations Observed Between DW-MRI Metrics of Techniques Other Than DKI and IVIM and Histological Indices Reported in the 54 Articles Included in This Review

MRI Metric	Correlation With Histology
SEM D_{SEM}	$r = -0.23, -0.52, -0.50, 0.64$ with nuclear, cytoplasmatic, cellular, and prostate stromal fractions[17]; $r = -0.57$ (Spearman's) with tumor cellularity[71]
SEM α	$r = -0.23, 0.22$ with cytoplasmatic fraction and nuclear-to-cytoplasm ratio[17]
VERDICT f_{ic}	$r = 0.90$ with fraction of HE stained area[54] (DDE-VERDICT)
VERDICT R	$r = 0.68$ with minimum Feret diameter of cells[54] (DDE-VERDICT)
IMPULSED d	$r = 0.92$ with in vitro mean cell diameter[64]; $r = -0.64, 0.52$ with percentage of CD3+ cells and all-cell mean diameter[65]
IMPULSED cellularity	$r = 0.81$ with histological cellularity[66]
IMPULSED f_{ic}	$r = 0.83$ with nuclear fraction[68]
QSI mean displacement	$r = -0.71, -0.67$ with nuclear-cytoplasmatic ratio and tumor cellularity[73]
QSI probability of zero displacement	$r = 0.79, 0.70$ with nuclear-cytoplasmatic ratio and tumor cellularity[73]
QSI propagator kurtosis	$r = 0.73, 0.74$ with nuclear-cytoplasmatic ratio and tumor cellularity[73]
QSI propagator full-width-at-half-maximum	$r = -0.51$ (Spearman's) with tumor cellularity[71]
RSI restricted fraction C_1	$r = 0.40$ with tumor grade[22]
HM-MRI epithelial fraction	$r = 0.93$ with histological epithelial fraction in the prostate[91]
HM-MRI lumen fraction	$r = 0.90$ with histological lumen fraction in the prostate[91]
HM-MRI stroma fraction	$r = 0.82$ with histological stroma fraction in the prostate[91]
DR-CSI epithelial fraction	$r = 0.74$ (Spearman's) with epithelial fraction in the prostate[99]
DR-CSI lumen fraction	$r = 0.67$ (Spearman's) with lumen fraction in the prostate[99]
DR-CSI stroma fraction	$r = 0.80$ (Spearman's) with stroma fraction in the prostate[99]
DR-CSI component fractions	The signal fraction of two components out of a 5-component spectrum correlated with tumor grade[100] ($r = 0.55$ and $r = -0.38$)

Weak correlations that in absolute value were lower than 0.2 were not included in the table. Values of r indicate Pearson's correlation coefficients, unless otherwise stated. Refer to section Advanced DW-MRI for the mathematical/physical foundations beyond each metric.

changes in the kurtosis excess K can be due to several, different independent changes in tissue microstructure, which may be difficult to tell apart, for example, changes in cell size, cell density, voxel heterogeneity, or water exchange.

Intravoxel Incoherent Motion

IVIM imaging was the focus of 20 articles[20,21,26–43] (Supporting Information Table S2). IVIM was originally proposed in 1986 by Le Bihan et al.[44]

Signal model: IVIM models two water pools (bi-exponential signal model). One describes signal from perfusion within randomly-oriented fluid-filled conduits (eg, capillaries, blood vessels, tubules), while the other true diffusion in nonvascular tissue.[44]

The overall magnitude signal attenuation in IVIM is written as

$$S = S_0\left((1-f)e^{-b\,D_t} + f\,e^{-b\,D^*}\right) \quad (2)$$

Above, S and S_0 are the same as in Eq. 21, f is the pseudo-diffusion (vascular) signal fraction (intrinsically relaxation-weighted), D_t is the tissue ADC, and D^* is the pseudo-diffusion ADC ($D^* \gg D_t$, ranging in 10–100 μm^2/msec), and can be notated as D or D_p, for "pure." Recently, Eq. (2)

has been extended to incorporate T2-effects[45] or to capture non-Gaussian diffusion[21,46] (joint IVIM-DKI).

Required diffusion encoding protocol: Body IVIM protocols typically require LTE with three mutually orthogonal gradient directions at various *b*-values. Low *b*-values (up to approximately 100 seconds/mm^2) are densely sampled, and additional *b*-values are acquired up to approximately 1000 seconds/mm^2. Signals from the three directions are averaged. The number of *b*-values used in the included articles ranged from 5 to 11.

Fitting methods: The choice of the fitting algorithm can significantly influence the quality of IVIM maps. Barbieri et al[47] compared six algorithms for IVIM fitting in abdominal imaging (Appendix C and Table 3). Bayesian probability (BP)-based fitting provides the highest precision and accuracy, and minimizes inter-reader/-subject variability. "Two-step fitting" is used in several studies,[20,21,37,40] but without further specifications. Two articles use Levenberg–Marquardt (LM) fitting.[30,35] Hecht et al[30] described the fitting procedure in detail.

Main histological correlates: The IVIM parameters of the nonvascular diffusion component are often employed as markers for cellularity, while pseudo-diffusion indices are used as markers of microvessel characteristics. In five articles,[20,27,31,32,40] a correlation between D_t and cellularity or related measures was found. However, in three articles,[21,29,30] no significant correlation was found. In one study both D_t and ADC were computed; the correlation with cellularity was stronger for D_t.[27] These findings were, however, not supported by four other studies.[21,26,29,31]

Conversely, f and D^* rarely correlated with cellularity, although some weak correlation with the level of necrosis was seen in Zhang et al.[42] In Xie et al,[43] a negative correlation between both f and D^* with liver cell size following hepatectomy was reported. Correlation with measures of vessel density was tested in 13 articles. In 10 articles, a significant correlation was reported,[29,33–37,39–42] while in three no correlation was found.[21,30,31] For example, f and D^* correlated positively with microvessel density (MVD).[41,42] D^* also correlated positively with the pericyte coverage index (PCI), while D_t correlated negatively with the vasculogenic mimicry (VM).[41]

Discussion: IVIM enables the joint estimation of tissue diffusion properties as well as characteristics of the local microvasculature, which may be useful in a variety of oncological applications, being abnormal vasculature a key characteristics of cancer. However, the practical implementation of IVIM in real-world clinical contexts faces a number of hurdles.

Firstly, a large number of *b*-value measurements are required. If one wants to accurately characterize both true-diffusion/pseudo-diffusion components, very long acquisitions may be required.

IVIM oversimplifies the true microstructure, as it models only two compartments, pooling all nonvascular contributions into a surrogate tissue component. Also, it does not account for intercompartment exchange,[48] compartment-wise relaxation,[45] and diffusion time dependence.[1] Because of this, IVIM parameters may be considered semi-quantitative.

Moreover, the included articles demonstrate clearly that there is currently a lack of standardization of both fitting procedure and acquisition protocol, which may be one of the leading factors behind the relatively poor reproducibility of IVIM metrics.

Finally, several studies[30–34] report that IVIM-parameters do not perform well in terms of repeatability (especially f, D^*). Flow-compensated acquisitions improve IVIM robustness,[49,50] but may not be available in all scanners. Efforts are also ongoing to optimize the clinical protocol and facilitate standardization.[51]

VERDICT

Eight articles reported on VERDICT[52–59] (Supporting Information Table S3). This model was originally proposed by Panagiotaki et al.[55]

Signal model: VERDICT is a biophysical, multi-compartment model fitted on DW-MRI measurements acquired at varying *b*-values, diffusion times and gradient directions with standard linear tensor encoding (PGSE). The model, developed on colorectal cancer xenograft mice,[55] has shown utility in vivo in prostate imaging[60] and in other contexts (eg, rhabdomyosarcoma).

VERDICT models three nonexchanging water pools:

- water in the intracellular space (restricted diffusion within spherical cells);
- water in the extracellular extravascular space (EES) (hindered diffusion in stroma and lumen, outside cells/vessels);
- water in the vascular compartment (pseudo-diffusion within blood vessels/tubules).

The total signal is written as

$$S = S_0\left(f_{\mathrm{ic}}\, S_{\mathrm{ic}}(d_{\mathrm{ic}}, R) + f_{\mathrm{EES}}\, S_{\mathrm{EES}}(d_{\mathrm{ec}}) + f_{\mathrm{vasc}}\, S_{\mathrm{vasc}}(d_{\mathrm{vasc}})\right) \quad (3)$$

Above, b is the *b*-value; $d_{\mathrm{ic,ec,vasc}}$ are the intrinsic diffusivity of the intracellular space (d_{ic}) and the EES/vascular ADCs ($d_{\mathrm{ec}}/d_{\mathrm{vasc}}$). R is cell radius, while the $f_{\mathrm{ic,EES,vasc}}$ are relaxation-weighted signal fraction ($f_{\mathrm{ic}} + f_{\mathrm{EES}} + f_{\mathrm{vasc}} = 1$). A recent article by Palombo et al[59] extended the VERDICT model (relaxation-VERDICT) to account for compartment-wise relaxation properties.

Required diffusion encoding protocol: VERDICT requires a rich PGSE protocol with several *b*-values and diffusion times (ie, varying Δ/δ). The different diffusion times may be sampled at the expense of varying the TE, a fact that has been

exploited in recent relaxation-VERDICT.[59] Sampling different diffusion times at different diffusion-weighting strengths provides sensitivity to cell size and cellularity due to restriction (intracellular space) or tortuosity (extracellular space), a phenomenon known as time-dependent diffusion (TDD).[1]

Recently, double diffusion encoding (DDE) VERDICT (made of two consecutive PGSE blocks; Appendix A) improved f_{ic} and R estimation.[54]

Fitting methods: VERDICT is generally fitted with f_{EES}, f_{ic}, R as free parameters ($f_{vasc} = 1 - f_{ic} - f_{EES}$) and $d_{ic,ec,vasc}$ fixed (and $d_{ic} = d_{ec}$), using an iterative optimization procedure.[52,55,57] The optimization is nonlinear, via LM algorithm (see Table C1 in Appendix C). VERDICT can also adopt different compartment-wise anisotropy, depending on the cancer type[55,57,61]: optimal compartment shape has been investigated with the Akaike information criterion (AIC).[53] Accelerated microstructure imaging via convex optimization (AMICO) fitting was used to speed up signal processing, without jeopardizing fitting accuracy.[52] An article[62] reported a method based on general adversarial networks (GANs) to synthesize VERDICT parameters from routinely acquired DW-MRI, suitable for ADC mapping. Methods of this type may be useful in clinical settings, but should be interpreted with care: microstructural information that is not encoded in the signal cannot be retrieved. The recent relaxation-VERDICT implementation was instead fitted using deep neural networks (DNNs),[59] resulting in lower metric variability, higher scan-rescan repeatability, and higher accuracy in parameter estimation.

Main histological correlates: All included articles were on prostate cancer, except for one on rhabdomyosarcoma[54] and one on colorectal cancer.[55] In the included articles, low/high f_{ic} was found to mirror areas of low/high cellularity,[53] a promising finding for potential applications in clinical trials. R was shown to be highly variable in areas of high lumen density. The quantitative comparison between VERDICT parameters and histology showed that VERDICT parameters are correlated with their histological counterparts,[55] and the level of agreement increases when tissue shrinkage due to histology processing is taken into account. Importantly, it can discriminate Gleason grades. The classical VERDICT implementation distinguishes benign prostate lesions from Gleason grade $3+3$, and $3+3$ from $3+4$. In additional, relaxation-VERDICT also distinguishes $3+4$ from $4+3$ or higher.[59]

Discussion: In three studies, a comparison was executed between VERDICT, ADC, IVIM, and DKI.[55,57,60] The most important benefit of VERDICT over the other techniques is that VERDICT describes specific histological factors, while the others provide surrogate indices of tissue microstructure.[60] Nonetheless, a joint quantitative benchmarking of these techniques against histology was executed in only one study, and further validation of VERDICT is required.

In VERDICT, a tailored acquisition is required to sample high b-values (up to ≈ 3000 seconds/mm^2) and various Δ, δ, and potentially TE in recent VERDICT extensions.[59] This results in demanding acquisitions, as for DKI.[55,62]

Concluding, VERDICT is a promising technique providing sensitive markers of specific histological properties, and variations in the acquisition/analysis (AMICO, DDE, GANs, DNN-fitting, joint diffusion-relaxation modeling), may strengthen its clinical feasibility. Its main advantage is that it attempts to disentangle independent factors that can contribute to the diffusion contrast, striving to provide quantitative estimates of relevant biophysical properties such as cell size or density. Its main disadvantage is that it relies on a biophysical model that makes strong assumptions on the underlying characteristics of the diffusion process (eg, it neglects water exchange; it assumes a fixed diffusivity in the intracellular compartment), which has not been fully validated yet. Moreover, it relies on a long acquisition protocol, which may be impractical in certain clinical contexts where scan time is limited.

IMPULSED

Seven articles report on IMPULSED[63–69] (Supporting Information Table S4), which is based on temporal diffusion spectroscopy (TDS), a framework that exploits TDD to resolve restriction lengths combining PGSE and oscillating gradient spin echo (OGSE). This method was proposed by Jiang et al.[66]

Signal model: IMPULSED models two nonexchanging compartments, describing intra-/extracellular water, that is,

$$S = S_0\left(f_{ic}\,S_{ic} + \left(1 - f_{ic}\right)S_{ec}\right) \quad (4)$$

where f_{ic} (also known as v_{in}) is the relaxation-weighted intracellular signal fraction, S_{ic}/S_{ec} intra-/extracellular signals. S_{ic} is modeled by diffusion within spheres of diameter d, with intrinsic cytosol diffusivity d_{ic}. S_{ec} is modeled as

$$S_{ec} = \exp(-b\,d_{ec}) \quad (5)$$

d_{ec} is approximately linear as a function of the OGSE frequency f[63–66] ($d_{ec} = d_{ec,0} + \beta f$), while it does not depend on δ/Δ in PGSE. A cellularity index can be obtained by combining d and f_{ic},[66] similarly to Panagiotaki et al.[60]

In the original IMPULSED, signal contributions from perfusion are ignored and intra-/extracellular exchange assumed to be negligible. In a study of Jiang et al,[63] a third compartment is added to describe the effect of vasculature. Li et al[67] investigate the influence of water exchange, suggesting that it can be ignored if the diffusion time is at least one order of magnitude smaller than the intracellular water lifetime τ_{in} (≥ 30 msec). Recently, water exchange was incorporated by Jiang et al[69] in IMPULSED. This improved fitting accuracy and provided additional τ_{in} and cell membrane permeability Pm estimates.

Required diffusion encoding protocol: IMPULSED utilizes LTE with both OGSE, probing ultra-short diffusion times maximizing sensitivity to cell size[66,68], and routine PGSE wave forms. To obtain microstructural information for common cell types, diffusion times in the range of approximately 1–70 msec are required.[63] Also, *b*-values up to approximately 1000 seconds/mm^2 are used.

Fitting methods: Fitting is performed via constrained nonlinear least square optimization. d_{ic} (intrinsic intracellular cytosol diffusivity) is fixed in most studies (eg, 3 μm^2/msec[63]) to increase precision.[63,64,68]

Main histological correlates: Comparisons to histological references were found for f_{ic} and d. f_{ic} is underestimated with respect to histology,[63,64,66,67,69] potentially due to unaccounted water exchange.[66,69] The cell size estimate d is less influenced by exchange and is moderately or strongly correlated with histology.[63–67,69]

Discussion: Similarly to VERDICT, IMPULSED relies on a multi-compartment model to disentangle key properties of intra-/extracellular diffusion, providing metrics of cytometry designed to be highly specific to histology. Practically, IMPULSED combines OGSE and PGSE to probe a wide range of diffusion times t_{diff} (approximately 1.7–52 msec) as this improves microstructural inference of cell size. However, such a requirement can hinder the practical implementation of the technique. The t_{diff} range that can be probed depends on the maximum available gradient strength,[65] and by the fact that OGSE may not be readily available in commercial scanners.[68]

In conclusion, IMPULSED is potentially clinically feasible, as long as the required gradient magnitudes are achievable and OGSE sequences are available. It provides histologically meaningful cell size indices (d), while accurate f_{ic} estimates are more difficult to obtain, especially if water exchange is not accounted for.

Stretched Exponential Model

In three papers, SEM, a technique developed by Bennett et al,[70] was mentioned,[17,33,71] despite not being the primary focus of the study (see Supporting Information Tables S1 and S5).

Signal model: SEM, a special case of fractional order diffusion, attempts to quantify diffusion heterogeneity by introducing a heterogeneity index α, such that

$$S = S_0 \exp(-(b\,D_{SEM})^{\alpha}) \quad (6)$$

S, S_0, and b have the same meaning as described earlier, while α ranges from 0 to 1. α close to 1 implies low diffusion heterogeneity (ie, diffusion approximately Gaussian; mono-exponential decay). Conversely, the closer α to 0, the more heterogeneous the diffusion process. D_{SEM} is the mean intravoxel diffusion coefficient.

Required diffusion encoding protocol: The protocol requirements are similar to those of DKI, namely, standard LTE with at least two nonzero *b*-values plus one or more non-DW images. In body imaging, three directions per *b*-value are typically acquired and averaged, and the diffusion time and TE are generally fixed for all *b*-values. The maximum *b*-value used in SEM is around 2000 seconds/mm^2.

Fitting methods: SEM parameter maps are typically obtained via nonlinear least squares fitting.

Main histological correlates: Two papers compared SEM to histological indices.[17,71] D_{SEM} shows similar negative histological correlation with cellularity. Correlation figures for α are weaker. Nonetheless, linear regressions that include both D_{SEM} and α predict histological cellularity better than D_{SEM} alone,[17] implying that α may carry sensitivity to microstructure.

Discussion: SEM provides a framework that enables the characterization of departures from Gaussian diffusion and mono-exponential decay through diffusion heterogeneity. SEM provides useful information on microstructure that generalizes routine ADC. However, it suffers from similar issues as the techniques described above. Firstly, its metrics are only semi-quantitative, as they may vary with varying diffusion protocols (eg, due to changes in the diffusion times). Moreover, SEM has an unphysical nature, as the exponent parameter α does not have any biophysical meaning.[72] Finally, it requires longer acquisition protocols and higher *b*-values than routine ADC mapping, due to its higher number of parameters. This comes at the price of reductions in SNR, as well as potentially higher susceptibility to motion.

Q-SPACE IMAGING. The q-space imaging (QSI) was the focus of two articles.[71,73] QSI is a phenomenological technique that recovers the spin displacement distribution due to diffusion, developed by the seminal work of Callaghan et al.[74]

Signal model: QSI enables the estimation of the probability density of diffusion displacement $\mathbf{r}$ due to diffusion over a time t ($p(\mathbf{r},t)$), known as *diffusion propagator*. The estimation of the propagator is made possible by the fact that the DW-signal measured as a function of the q-value $\mathbf{q} = \gamma\,\delta\,G\hat{\mathbf{g}}$ (with G, δ, and $\hat{\mathbf{g}}$ being the gradient strength, duration, and direction) at a fixed gradient separation Δ in the short gradient pulse limit ($\delta \ll \frac{L^2}{D_0} \ll \Delta$,[75] where L is the compartment size and D_0 the intrinsic diffusivity), is the Fourier transform of $p(\mathbf{r},t=\Delta)$. This can be estimated by inverse Fourier-transforming DW measurement sets $S(q,\Delta)$,[3,76] that is,

$$p(\mathbf{r},\Delta) = F^{-1}\{S(\mathbf{q},\Delta)\} \quad (7)$$

Required diffusion encoding protocol: For QSI, rich protocols based on LTE PGSE are typically required. A high

number of measurements is required to sample the q-space and enable accurate inverse Fourier transformation. For example, in earlier studies,[71,73] 32 *b*-values up to 7163 seconds/mm^2 were used.

Fitting methods: The propagator in Eq. 7 is estimated via practical numerical implementations of inverse Fourier transformation, such as the fast inverse Fourier transform.[71] Ad hoc methods have also been proposed in the literature for the estimation of the propagator and of its salient properties, such as diffusion spectrum imaging (DSI, 2005),[77] or mean apparent propagator MRI (MAP-MRI, 2013).[76] Multiple metrics can be used to characterize $p(\mathbf{r},\Delta)$, for example, mean displacement (MD) or mean squared displacement (MSD),[73] measurement of displacement probability (such as the probability of zero displacement (PZD[73]), or the return-to-origin/axis/plane probabilities (RTOP, RTAP, RTPP) from MAP-MRI[76]), or the kurtosis[73] of the full-width-at-half-maximum (FWHM) of the propagator itself.[71]

Main histological correlates: In an earlier study,[73] MD correlated negatively with nuclear cytoplasmatic ratio and tumor cellularity, while PZD and kurtosis correlated positively with both features. In another study,[71] the FWHM and its skewness correlated negatively with cellularity and skewness of cellularity, respectively.

Discussion: QSI offers the advantage of reconstructing in full the diffusion propagator, enabling the characterization of several different features of non-Gaussian diffusion. The included articles demonstrate that QSI is sensitive to changes in microstructure.[71,73] Specifically, measures of water displacements derived from the propagator correlate with cellularity/cell density. Potential drawbacks of QSI are that its metrics are surrogate markers with limited biological specificity, since several different, independent factors can cause alterations of the propagator. Moreover, the propagator is intrinsically diffusion-time dependent, implying that QSI metrics are semi-quantitative, being protocol dependent. Finally, QSI acquisitions are more demanding than those required for ADC measurement.

MRI-CYTOMETRY. MRI-cytometry is a two-pool intra-/extracellular biophysical framework for mapping cell size distributions, proposed by Xu et al,[78] which is one of the articles selected in this review (see also Supporting Information Table S5).

Signal model: The MRI-cytometry model is a two-compartment model that describes the signal as arising from the sum of intracellular and extracellular, extravascular components, without intercompartment exchange, that is,

$$S = S_{ic} + S_{ec} \tag{8}$$

Both intra-/extracellular signals are described as the sum of a continuous distribution of spin packets with fixed properties. For a *b*-value b and a diffusion time τ, the these are written as

$$S_{ic} = \int_{d_{ic}} \int_{R} \rho_{ic} \frac{8\pi}{3} R^3 a_{ic}(d_{ic},R)\, P(d_{ic},R)\, dd_{ic}\, dR \tag{9}$$

for intracellular signal and

$$S_{ec} = \int_{d_{ec,0}} \int_{\beta} \rho_{ec}\, e^{-b(d_{ec,0}+\beta/\tau)}\, P(d_{ec,0},\beta)\, dd_{ec,0}\, d\beta \tag{10}$$

for the extracellular signal. Above, d_{ic} is the intrinsic intracellular diffusivity, $d_{ec,0}$ is the asymptotic extracellular ADC, R is the cell radius, β is the extracellular TDD factor, ρ_{ic} and ρ_{ec} are the unit signal per unit volume coming from the intracellular and extracellular compartment, respectively, and $a_{ic}(d_{ic},R)$ is the characteristic signal of a cell with radius R and cytosol diffusivity d_{ic}.

Required diffusion encoding protocol: As IMPULSED, MRI-cytometry utilizes LTE with both OGSE and PGSE wave forms. The technique has been demonstrated in vivo on a clinical system using diffusion times τ of 70, 10, and 5 msec, with the highest b being of 1800, 1000, and 300 seconds/mm^2 for each τ.

Fitting methods: The MRI-cytometry model is fitted after constructing a discrete dictionary of candidate intra-/extracellular signals, following a two-step regularized nonlinear least square procedure.[78] This provides estimates of the joint probability density functions $P(d_{ic},R)$ and $P(d_{ec,0},\beta)$ in each voxel. Integrating $P(d_{ic},R)$ over d_{ic} enables mapping the cumulative cell size distribution, whose peaks can be used to identify different cell populations with remarkably different average cell sizes.

Main histological correlates: The authors report a good match between cell size estimates and references from cell cultures in vitro. However, correlation coefficients were not calculated, owing to the small sample size.

Discussion: MRI-cytometry is essentially a more complex implementation of IMPULSED. The technique can potentially provide more in-depth information on the different cell types present in a voxel (eg, small lymphocytes vs. larger cancer cells), as it enables recovering a full cell size distribution, rather than a single cell size index per voxel, as IMPULSED. However, the more complex model comes at the expenses of more complex parameter estimation, which is even more prone to instabilities, and requires regularization. Finally, similarly to IMPULSE, the technique requires combining LTE with OGSE and PGSE wave forms. The former are typically not available in vendor-provided diffusion sequences, and may therefore be a hurdle for its practical clinical implementation.

RESTRICTION SPECTRUM IMAGING. Restriction spectrum imaging (RSI) was the focus of two articles included in this

review[22,79] (Supporting Information Table S5). RSI was proposed in brain imaging by White et al.[80]

Signal model: The method models the DW-signal as arising from a distribution of diffusion tensor components. The components with the slowest diffusion are used as proxies for water restricted within cells. Different RSI implementations vary depending on the number/characteristics of the components. One of the RSI articles included in this review used three-component for discriminating rectal cancer grades,[22] that is,

$$S = S_0\left(C_1 e^{-b\,D_1} + C_2 e^{-b\,D_2} + C_3 e^{-b\,D_3}\right)\ s.t. D_1 < D_2 < D_3 \quad (11)$$

where $C_{1,2,3}$ are relaxation-weighted signal fractions for restricted, hindered, and free water, while $D_{1,2,3}$ ($D_i < D_{i+1}$) their ADCs.

Required diffusion encoding protocol: RSI can be performed at fixed diffusion time and it has been implemented with protocols as short as 5 minutes. The method has been demonstrated using LTE PGSE with maximum *b*-values as low as 1000 seconds/mm^2 in Yamin et al[79] and 2000 seconds/mm^2 in Xiong et al,[22] that is, using the same protocols that one could employ for DKI.

Fitting methods: Equation 11 is typically fitted using nonlinear least square approaches. During fitting, the ADCs of the different diffusion components are not estimated, but rather fixed to characteristics values. For example, in Xiong et al[22] the following values were used: $D_1 = 0.5$ μm^2/msec (restricted diffusion), $D_2 = 1.3$ μm^2/msec (hindered diffusion), $D_3 = 3.0$ μm^2/msec (free water diffusion). After fitting, signal fraction maps can be standardized in the form of *z*-scores using reference values from healthy tissue, for example, from the healthy prostate, as in Yamin et al.[79]

Main histological correlates: Yamin et al[79] used RSI to estimate cellularity in prostate cancer, detecting variations of Gleason grade within a single tumor. Similarly, in Xiong et al,[22] the restricted signal fraction C_1 correlated with rectal cancer grade.

Discussion: RSI is a promising technique that attempts to disentangle different sub-voxel signal sources, providing signal fraction maps designed to be specific to characteristics cellular components. The technique is based on a multi-component representation that can fitted more easily than multi-compartment models such as IMPULSED, being the properties of such components fixed (ie, prespecified D_i values). However, this comes at the price of potential biases in the signal fraction maps, since the characteristics ADCs of the different sub-voxel components are likely to vary on a voxel-by-voxel basis. Moreover, RSI modeling does not take into account explicitly the diffusion time, implying that its metrics are likely to be protocol dependent. Regarding the acquisition, RSI requires more complex protocols than routine ADC measurement. Nonetheless, it has been demonstrated with compact scan times under 10 minutes, which offer promise for clinical translation.

MC SIMULATIONS FOR MICROSTRUCTURAL MAPPING FROM CLINICAL DW-MRI.

One article[81] (see also Supporting Information Table S5) investigated microstructural parameter estimation from clinical DW-MRI informed by MC simulations in skull-base chordoma cases treated with radiotherapy.

Signal model: The technique essentially aims to map several ADC values obtained from different sub-protocols of multi *b*-value clinical DW-MRI, to microstructural parameters that are more specific to the underlying tissue histology: cellular radius R, cell volume fraction f_{ic}, cell diffusivity d_{ic}, and apparent cellularity ρ_{app}.

Fitting methods: The mapping (ADC$_1$, …, ADC$_N$) → (f_{ic}, R, d_{ic}, ρ_{app}) is achieved by comparing voxel-wise ADC maps to sets of synthetic, candidate ADCs values generated via Monte Carlo simulations. The comparison involves multiple steps, and accounts explicitly the uncertainty of the estimation of each microstructural parameter due to noise. Monte Carlo simulations were performed within synthetic cancer micro-environments in the form of 3D meshes.

Required diffusion encoding protocol: The approach has been demonstrated with routine PGSE LTE, which included three *b*-values (50, 400, and 1000 seconds/mm^2).

Main histological correlates: Microstructural maps were related to the cancer aggressiveness as measured by Ki-67 immunohistochemistry. All estimated tissue parameters differed between more vs. less proliferative tumors (ie, high Ki-67 vs. low Ki-67 immunostain).[81] Moreover, statistical survival models that combined all microstructural parameters could predict the risk of progression following radiotherapy with high accuracy.

Discussion: The approach presented by Morelli et al[81] is promising in that it enables clinically feasible estimation of microstructure metrics without any further assumptions than those that go into the simulations.[82] The framework relies on simulations of diffusion that can be performed on synthetic cancer micro-environments, and that can therefore incorporate unprecedented levels of microstructural details. On the one hand, this removes the need for developing analytical expressions of the signal based on over-simplified geometric models of the tissue (eg, modeling cells as spheres, as in VERDICT or IMPULSED). On the other hand, the approach can potentially enable the mapping of indices of cell heterogeneity, for example, measures of dispersion in cell size or morphology. Despite its potential, the method remains complex to be deployed in practice, since most centers may not have the capabilities to run Monte Carlo simulations of the very specific DW-MRI sequences being used at the center. The approach has shown potential clinical utility, but the

microstructural parameters have still to be validated by comparisons to their direct counterparts from histology.

MULTIDIMENSIONAL DIFFUSION MRI. Multidimensional diffusion (MDD) MRI, also known as *b*-tensor encoding or q-space trajectory imaging, makes use of generalized diffusion gradient wave forms.[4] The approach, pioneered in vivo by Westin et al[4] after preclinical development by Topgaard et al,[83,84] was investigated by Naranjo et al,[85] an article included in this review (Supporting Information Table S5).

Signal model: In MDD, diffusion-weighting is described in terms of a *b*-tensor **B**, rather than by scalar *b*-values. **B** is defined as

$$\mathbf{B} = \int_0^{\mathrm{TE}} \mathbf{q}(t)\,\mathbf{q}(t)^{\mathrm{T}} dt \qquad (12)$$

where $\mathbf{q}(t) = \gamma \int_0^t \mathbf{g}(\xi) d\xi$, with the diffusion gradient $\mathbf{g}(t)$ free to change its direction during encoding. This sensitizes measurements to different diffusion directions at once, probing a new contrast that is not accessible to PGSE,[86–88] and disentangling heterogeneity in isotropic diffusivity from diffusion heterogeneity caused by anisotropy. Different methods have been proposed to analyze data acquired with *b*-tensor encodings beyond standard LTE PGSE or OGSE. These typically express the DW signal in terms of a continuous distribution of microscopic domains, each characterized by a specific diffusion tensor,[89] that is,

$$S(\mathbf{B}) = S_0 \int P(\mathbf{D})\, e^{-\mathbf{B}:\mathbf{D}} d\mathbf{D} \qquad (13)$$

Above, **B** is the acquisition *b*-tensor, **D** is the diffusion tensor of the generic diffusion component, $P(\mathbf{D})$ is the diffusion tensor distribution (DTD), and: denotes the double inner product between the diffusion-/*b*-tensors.

Required diffusion encoding protocol: MDD-MRI protocols typically entail a variety of *b*-values sampled with different *b*-tensor encoding shapes, for example combinations of LTE, spherical tensor encoding (STE), and planar tensor encodings (PTE). While STE and PTE may not be available off-the-shelf in vendor-provided DW-MRI sequences, several works have now developed robust implementations across multiple system platforms and manufactures, which have shown excellent stability and reproducibility.[90]

Fitting methods: The *b*-tensor encoding parametric maps are typically recovered by parametrizing the signal as a function of different features of the DTD, depending on the tissue of interest. For example, the signal can be parametrized as function of the overall mean diffusivity ($\overline{D}$) and the anisotropic and isotropic diffusional variance (V_A and V_I),[90] or via cumulant expansions of the DTD.[4] Fitting is then performed via nonlinear least square optimization, and once the DTD parameters have been recovered, other microstructural parameters of interest can be derived analytically, for example, microscopic fractional anisotropy.

Main histological correlates: Naranjo et al[85] used LTE and spherical-tensor encoding to obtain metrics as D_{iso} (isotropic diffusivity) or $D_{\Delta 2}$ (shape parameter of diffusion anisotropy, similar to V_A) of the various tensors making up the DTD. Cancer and healthy tissue differed according to nearly all DTD metrics. However, histological data were only assessed mainly qualitatively, as also done, for example, in the prostate.[86]

Discussion: MDD MRI has expanded the capabilities on in vivo DW-MRI, giving access to new diffusion contrasts that cannot be probed with conventional diffusion imaging. These may enable disentangling subtle microstructural differences that would be indistinguishable in conventional PGSE, ultimately providing useful biomarkers in several types of body cancer. Despite its potential, at present the practical clinical use of MDD is challenged by the limited availability of *b*-tensor encoding as an off-the-shelf product sequence. Moreover, *b*-tensor DTD metrics, while surely promising, are phenomenological indices that are sensitive to different features of the underlying microstructure. Histological validation is ongoing in a variety of clinical contexts[25] to confirm their specificity, and to rule out confounding factors that have not been account for yet. Finally, it should be noted that MDD also comes with some challenges. For example, it has proven difficult define exactly the sequence effective diffusion time in presence of irregular, oscillatory gradient wave forms, as those required for the efficient implementation of STE and/or PTE. This implies that strong differences in diffusion time across different *b*-tensor implementations, if not accounted for, may confound the values of DTD metrics across scanners, and could therefore hinder the deployment of these metrics as quantitative markers in clinical settings.

HYBRID MULTIDIMENSIONAL MRI. Two papers used HM-MRI,[91,92] proposed by Chatterjee et al[93] (see Supporting Information Table S6).

Signal model: HM-MRI models the signal as the sum of lumen, stroma, and epithelium components:

$$S = S_0 \left(\sum_{n=1}^{3} V_n\, e^{-b\,\mathrm{ADC}_n - \frac{\mathrm{TE}}{T_{2n}}} \right) \qquad (14)$$

Above, V_n, $\mathrm{T2}_n$, and ADC_n are signal fractions, T2, and ADC of lumen, stroma, and epithelium water ($n = 1,2,3$), which are fitted by imposing upper/lower bounds.[93]

Required diffusion encoding protocol: HM-MRI requires standard LTE PGSE acquisitions. Images at multiple *b*-values and multiple echo times TE are used, with three or more directions per unique (*b*,TE) value, which are averaged. The maximum *b*-value required for HM-MRI is around 1500 seconds/mm^2. Regarding TE, values as high as 200 msec or more are needed to appreciate the T2-decay of lumen water, known to feature a much longer T2 than the stromal or epithelial components. HM-MRI has been demonstrated using at least nine unique (*b*,TE) acquisitions.[93]

Fitting methods: Equation14 is fitted via nonlinear least square optimization, imposing upper/lower bounds on compartment-wise ADC and T2 values.[93] For example, the lumen signal component is assigned the highest ADC and longest T2, while the epithelial signal component the lowest ADC.

Main histological correlates: Tissue composition changes were observed in presence of prostate cancer and reflected different histological grades. For instance, an increased epithelium and reduced lumen fractions were found in tumors.[91] HM-MRI fractions of lumen, epithelial, and stromal signal agree excellently with counterparts derived from histology,[91] and matched well with expert interpretation.[92]

Discussion: HM-MRI is a diffusion-relaxometry method, which aims to resolve diffusion and relaxation properties jointly in each voxel through multi-contrast readouts.[94,95] Joint diffusion-relaxometry imaging may be beneficial when TR or TE are changed as part of the diffusion encoding protocol (eg, due to restrictions imposed by MRI manufacturers[60]), or to account for the TE-dependence of multi-compartment signal fractions.[45] Results from the papers included in this review suggest that HM-MRI offers promise from clinical translation, given its excellent agreement with histology and its easy-to-implement protocol, requiring approximately 10 minutes. However, HM-MRI suffers from similar issues as methods such as DKI or RSI: its metrics may be protocol-dependent, since they 1) do not take into account sequence parameters such as the diffusion time (which may vary across *b*-values due to changes in TE), and 2) rely on assumption on the characteristics ADC and T2 of the different prostate components, which are unlikely to hold across all prostate voxels. Finally, the long TE required by HM-MRI jeopardizes the overall SNR, and acquisition protocols are more demanding than those required for ADC measurement.

DIFFUSION-RELAXATION CORRELATION SPECTRUM IMAGING. Diffusion-relaxation correlation spectrum imaging (DR-CSI) was proposed by Kim et al[96] and de Almeida Martins and Topgaard,[97] after pioneering DR-CS work in spectroscopy in the early 2000s.[98]

Two papers included in this review focused on DR-CSI[99,100] (Supporting Information Table S6).

Signal model: In DR-CSI, no predefined number of compartments has to be defined,[99] being the signal dependent on a continuous ADC-T2 distribution $p(\mathrm{ADC}, \mathrm{T2})$, that is,

$$S(b,\mathrm{TE}) = S_0 \int_0^\infty \int_0^\infty p(\mathrm{ADC},\mathrm{T2})\, e^{-b\,\mathrm{ADC}-\frac{\mathrm{TE}}{\mathrm{T2}}}\, d\mathrm{ADC}\, d\mathrm{T2} \quad (15)$$

Required diffusion encoding protocol: DR-CSI is similar to HM-MRI, in that it requires multiple LTE with PGSE wave forms, acquired at varying *b*-values and *TE*. In body imaging the technique has been demonstrated on ex vivo prostate scanned on a clinical system with 16 unique (*b*,TE) encodings,[99] for a maximum *b* of 1500 seconds/mm^2 and maximum TE of 120 msec.

Fitting methods: $p(\mathrm{ADC}, \mathrm{T2})$ (the ADC-T2 spectrum) can be recovered via inverse-Laplace transformation or related numerical approaches.[94] In a previous study,[99] $p(\mathrm{ADC}, \mathrm{T2})$ non-negative nonlinear least square regression with total variation spatial regularization was used. Peaks in $p(\mathrm{ADC}, \mathrm{T2})$ provide component fraction maps and characteristic ADC/T2.[94,99] Other fitting approaches are based on defining a prespecified number of normative spectral component, for example drawing regions-of-interest in tumors and/or normal tissue. The fraction of each component is then mapped voxel-wise using regularized spectral analysis with cross-subject spectral standardization.[100]

Main histological correlates: In Zhang et al,[99] which focused on prostate imaging, three signal components were detected, and found to correspond to histological epithelium, stroma, and lumen, with promising significant positive correlations. The study only focused on ex vivo data, and in vivo confirmation is required. Conversely, Dai et al[100] tested whether DR-CSI enables the noninvasive grading of clear cell renal cell carcinoma. The authors identified five different ADC-T2 spectra in the kidney, and mapped the signal fraction of these spectra voxel-by-voxel. Two of these signal fraction maps correlated with cancer grade from histopathological assessment of HE-stained sections obtained from nephrectomy.

Discussion: Considerations for DR-CSI are essentially equivalent to those discussed above for HM-MRI. The method is promising as it enables disentangling different water pools within a voxel. As compared to HM-MRI, DR-CSI does not make any assumption on the number and characteristics of ADC-T2 component, and can therefore provide higher specificity to biology: peaks in the ADC-T2 spectrum can be assigned to specific components (eg, to stroma, rather than epithelium) by means of pilot MRI-histology correlation analyses. However, resolving a full ADC-T2 spectrum is inherently more challenging, so this could come at the expenses of higher metric variability and/or blurring of information due to the strong regularization required for stable fitting. Finally, as for HM-MRI, DR-CSI requires

very long TE, which reduce SNR, and does not take into account changes in diffusion time during the acquisition (likely to happen in clinical systems owing to changes in TE). Ultimately this may confound at least in part the recovered ADC-T2 spectra, and lead to sub-optimal protocol-dependent metrics. However, this is merely a practical limitation owing to current practices in sequence design, which could be easily mitigated by scanner software upgrades.

mpMRI-Based AI

Finally, one paper reported on methods predicting histology indices from multi-parametric MRI (mp-MRI)[101] with AI (Supporting Information Table S7).

Signal model: This approach is general and flexible, in that it relies on training AI systems that predict histological properties directly from mpMRI images and, potentially, easy-to-get parametric maps, as for example routine ADC as provided by the MRI scanner as part of any clinical mpMRI implementation.

Required diffusion encoding protocol: The approach has been demonstrated on prostate mpMRI, which includes high-resolution anatomical T2-weighted images, DW-MRI with at least one nonzero *b*-value for ADC calculation, plus, potentially, other contrasts, such as T1-weighted anatomical imaging and/or dynamic contrast-enhanced (DCE) MRI.

Fitting methods: Histological images were coregistered to MRI and AI algorithms such as DNNs were trained to map MRI directly to histology. The user potentially does not require to perform any DW-MRI signal model fitting, since simple parametric maps such as ADC provided by the scanner in clinical mpMRI can be stacked as inputs of the DNNs.

Main histological correlates: Sun et al[101] estimated prostate cell density from mp-MRI with a generalized additive model (GAM).

Discussion: The study shows promising MRI-histology correlations, with minimal requirements in terms of the diffusion protocol. Nevertheless, the approach is challenged by several issues that are typically encountered in AI-based methods. First of all, large, high-quality datasets of colocalized mpMRI and histology data—per se very difficult to obtain—are needed to robustly train the AI systems. These should include mpMRI protocols acquired with a variety of approaches, field strengths, resolutions, contrasts, and others, and in a variety of clinical contexts, to ensure generalizability of the results. Secondly, extensive validation is needed to ensure that the trained AI system do not provide histology predictions with hallucinated features.

Discussion

Summary

We reviewed systematically the state-of-the-art of advanced DW-MRI in body imaging in cancer (beyond the central nervous system, ie, mainly abdominal/pelvic imaging; and beyond routine ADC), analyzing its value in tissue microstructure assessment. Many different techniques were found, with the most common being IVIM, DKI, VERDICT, and IMPULSED, and other gaining momentum, for example, MDD or diffusion-relaxation MRI. All these methods add additional degrees of freedom to routine diffusion protocols, increasing the measurement space so that more microstructural information can be encoded in the signal, as illustrated in Fig. 5. This is done by acquiring extra *b*-values (eg, IVIM, DKI, RSI), by varying diffusion times (eg, VERDICT, IMPULSED) or TE (eg, HM-MRI), or by using new gradient wave forms (eg, MDD). These approaches have their own strengths and limitations, and their clinical feasibility depends on requirements for nonstandard sequences, maximum *b*, or scan time. A practical example of a rich acquisition in this high-dimensional measurement space is provided in Fig. 6. The figure shows a breast cancer liver metastasis imaged at 3 T with a diffusion-relaxation protocol, where four different *b*-values are acquired with LTE at three different echo times TE. The images reveal faster signal decay with increasing *b*-value within the tumor core, likely indicative of necrotic areas, which are surrounded by active tumor.

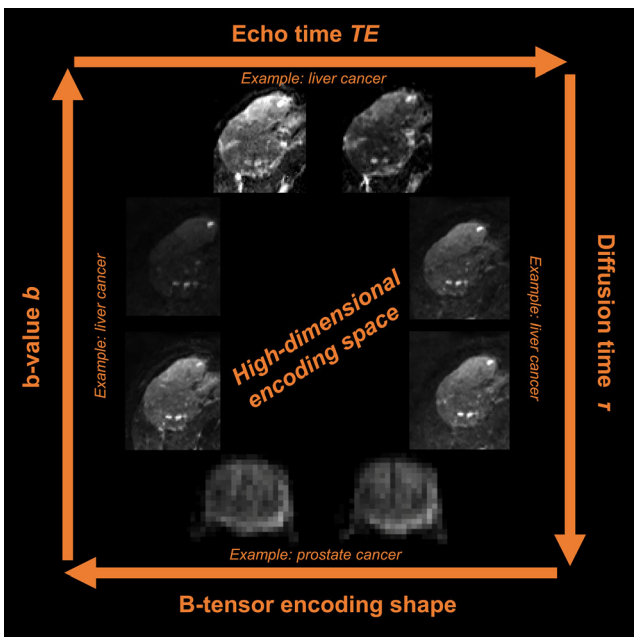

FIGURE 5: Illustration of the acquisition space exploited in advanced DW-MRI techniques. The figure illustrates the main acquisition parameters that can be varied to generate high-dimensional multi-contrast image sets in advanced diffusion imaging, that is, changes in *b*-value (overall diffusion-weighting strength), *b*-tensor encoding shape (eg, planar, spherical, or routine linear encoding), diffusion time, as well as potential changes in echo, inversion, or repetition times for joint diffusion-relaxation imaging. Changes in *b*-value, diffusion time and echo time are illustrated with a hepatocellular carcinoma (primary liver cancer) case, scanned at 1.5 T. Changes in *b*-tensor encoding shape are instead illustrated with a prostate cancer case, scanned at 3 T. The prostate images have been adapted from fig. 2 of reference 86 which was published in open access form under a CC-BY Attribution 4.0 International license.

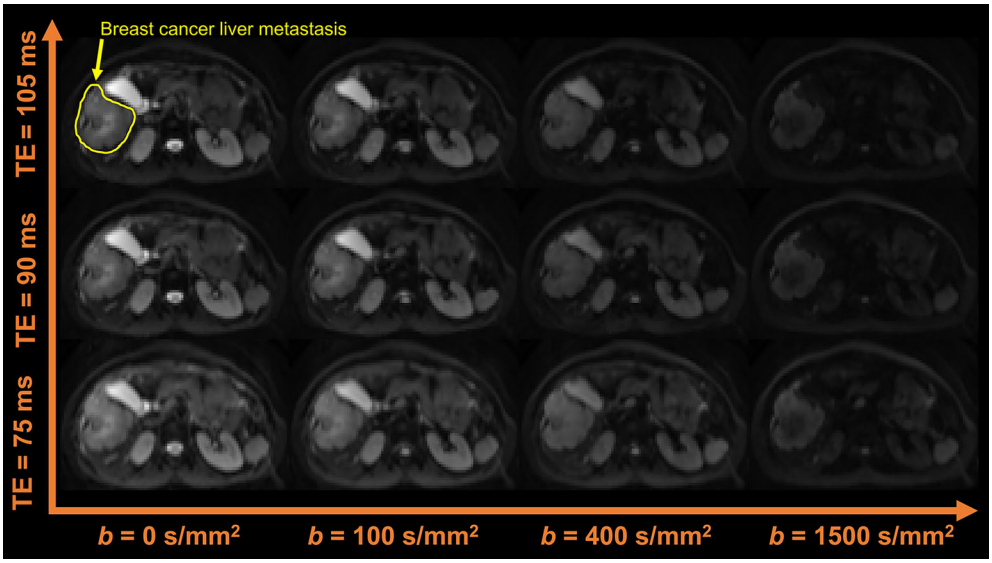

FIGURE 6: Example of a rich, advanced DW-MRI acquisition in body cancer. The figure shows a diffusion-relaxation acquisition performed at the level of the abdomen with a 3 T system, to image a breast cancer liver metastasis. The diffusion protocol features the acquisitions of multiple *b*-values *b* with LTE, each acquired independently at several echo times TE.

Routine DW-MRI: ADC Mapping

ADC mapping was not included in this review, as it is extensively covered elsewhere. Our article focuses explicitly on methods that go beyond routine ADC measurement, and for which histological validation has been carried out.

This explains the number of articles included in the review, that is, 54.

ADC is, by construction, a surrogate, semi-quantitative metric that pools into one number several microstructural sources of diffusion contrast. Moreover, its actual numerical value depends strongly on the interaction between the DW-MRI acquisition protocol and the underlying microstructure, making it a semi-quantitative, protocol-dependent index. Despite these well-known limitations, ADC has also shown some potential clinical utility in several oncological applications, some of which are briefly discussed below for the benefit of the readership. For example, DW sequences are now routinely included in genitourinary system imaging, with applications in the female pelvis, imaging of uterus and ovary, as well as prostate, bladder, penis, testis, and kidney.[102] DW acquisitions routinely come with scanner-computed ADC maps; these aid the visual interpretation of the expert radiologist beyond anatomical sequences, and are used, in some cases, to calculate cut-off values that can aid the differentiation of different types of cancers (eg, leiomyomas from uterine sarcomas[102]). Useful ADC cut-offs have also been proposed to distinguish metastatic vs. nonmetastatic lymph nodes in breast cancer with high reliability,[103] while the detection of early ADC increases following chemo-/radiotherapy in esophageal cancer were predictive of response.[104] In prostate imaging, DW imaging and ADC maps are now routinely included as part of the Prostate Imaging Reporting and Data System (PI-RADS),[105] a structured mpMRI report used in the treatment-naive prostate to study potentially malignant lesions. ADC has been found to be moderately correlated with cancer grade as assessed by the Gleason score,[106] although at present there are still no, widely accepted ADC cut-offs that can be used to classify prostate lesions as malignant.[107] Such associations with Gleason score are in line with related findings on cancer cellularity: ADC has been widely reported to correlate with tumor cellularity.[108] However, while characteristics beyond cell density should be taken into account when interpreting ADC changes,[109] since ADC has been reported to correlate to a variety of histological properties, such as tumor-stroma ration, cell count, proliferation indices from Ki-67 immunostains, or number of tumor-infiltrating lymphocytes in several types of cancer of the liver.[110] From the more practical point of view of the MRI acquisition, efforts are also ongoing in terms of standardization of protocols for ADC calculation: guidelines in term of *b*-value choice, for example, are provided as part of structured reports such as PI-RADS[105] for the prostate or Oncologically Relevant Findings Reporting and Data System (ONCO-RADS) for whole-body imaging.[111] Consensus guidelines have also been published, as for renal and breast DW-MRI.[112,113]

Advanced DW-MRI

Given the limitations of standard ADC mapping discussed above, current efforts of the DW-MRI community focus on developing novel techniques capable of providing metrics that are not only sensitive, but also highly specific to tissue features relevant in cancer. For this purpose, different biophysical signal models and/or phenomenological signal representations have been developed in a variety of body

imaging contexts (see Fig. 4 as well as Appendix A for some basics principles of DW-MRI physics and signal modeling). These are typically based on analytical expressions that parametrize the signal as a function of the diffusion-encoding gradient timing and amplitude, as well as of tissue parameters of interest. DW-MRI then attempts to solve an inverse problem, that is, to infer the unknown tissue parameters in each voxel from sets of signals measured at varying diffusion encodings. To solve this task, several different estimation techniques are used, such as nonlinear least squares fitting. However, the solution of this inverse problem is generally ill-posed: different combinations of tissue parameters can explain the DW measurements equally well. This issue is exacerbated by scarce acquisition protocols, which lead to degeneracy (measurement sets effectively lack specificity toward all microstructure parameters[114,115]). To cope with this problem, the go-to solution has been to fix some tissue parameters to predetermined values. While this may increase estimation robustness, it also leads to biases when the microstructure does not conform to modeling assumptions. The bias is unlikely to prevent a correlation between model parameters and a wide range of microstructures. However, subtle, pathological changes may produce a response in the constrained parameters that does not reflect the actual microstructural alteration. Ultimately, this can lead to inflated believes in the validity of constrained models. Recently, DNNs are becoming increasingly popular to solve this inverse problem.[59,62,116] Nonetheless, even with AI it is not possible to retrieve the microstructural information that is not encoded in the signal.[117] This implies that DW-MRI parametric maps obtained through DNNs should always be interpreted with care: unless specific strategies to map prediction uncertainty are implemented, DNNs always produce confidently an output, which could then exhibit *hallucinated* features in presence of unexpected inputs, as these will be mapped to the closest examples seen during the training stage.

MRI-Histology Agreement

Histological validation is imperative to demonstrate the sensitivity and biological specificity of any new DW-MRI metric. To this end, the voxel-by-voxel comparison of spatially matched MRI and histology is ideal. However, obtaining this type of data in vivo is challenging, as it would require access to entire slabs of excised tissue, for example following surgery.[118] Alternatively, tissue can also be imaged ex vivo, following excision. Nonetheless, in this case it would lack perfusion, and in both cases, microstructural changes occur as a consequence of fixation. Importantly, DW-MRI maps are typically compared to tiny two-dimensional sections of histological material (MRI slice thickness ~0.5–2.5 mm; histology sectioning of ~4–20 μm). As a consequence, portions of tissues that contributed to the MRI signal are not included in histological analyses. This may explain, at least in part, why within-sample MRI variations are not always mirrored by histology, despite overall strong MRI-histology between-sample agreement.

Another challenge is the fact that distributions of microstructural domains exist within a voxel. As a consequence, some MRI metrics may depend on the image resolution[119] (the lower the resolution, the more heterogeneous the voxel content). Also, this means that nontrivial histological features can be encoded in the DW signal. For example, DW-MRI cell size estimates are biased toward the largest cells, as these feature stronger time dependence, contain more water than smaller cells, and since the smallest cells may not even be distinguishable (4–8 μm is the intrinsic cell size resolution limit with clinical systems[120]). For this reason, comparing DW-MRI cell size maps to the arithmetic mean of histology cell sizes l (ie, $\langle l \rangle$) may provide lower agreements than comparisons to other statistics emphasizing the largest cells, for example, $\left(\frac{\langle l^7 \rangle}{\langle l^3 \rangle}\right)^{\frac{1}{4}}$.[15]

Nevertheless, all in all the articles in this review suggest that measuring key cancer properties throughout the body in clinical setting may be feasible, that is, vascularization through IVIM-like approaches, and cell size/cellularity with VERDICT, IMPULSED, MDD, and more. The analyzed methods, while not always accurate, retain sensitivity to key microstructural properties, and may provide noninvasive readouts useful in oncology.

Challenges

Despite the potential of the reviewed methods, challenges remain.

Firstly, the variety of acquisition protocols encompassed in the review highlights the lack of standardization of advanced DW-MRI. While a truly quantitative MRI method should provide metrics that are invariant to the acquisition protocol, in practice the number of microstructural parameters that can be estimated depends on the measurements available. As a consequence, harmonization (either prospective, or retrospective[121]) may be required before the new biomarkers can be considered truly quantitative. In this respect, we point out that certain interscanner differences are intimately related to the specifics of the acquisition, and are not only expected, but they actually encode microstructural information. For example, the overall ADC is approximately equal to the average of the ADCs of the different intravoxel compartments, weighted by a TE-dependent fraction, that is, $\mathrm{ADC}(TE) \approx \sum_i f_i(\mathrm{TE})\,\mathrm{ADC}_i$. Therefore, two ADCs obtained at two very different TE may also be very different between each other, due to inherently different T2-weighting. Harmonizing these types of differences requires extra care, as it could blur information about disease processes.

Another challenge is related to scan times being longer than what is feasible in hospital settings. DW-MRI is only one of the several contrasts that are probed during an imaging session, where each contrast typically takes no more than 10 minutes. Future work is required to make the latest DW techniques feasible with ultra-short acquisitions, potentially exploiting AI.

Furthermore, the review has highlighted that DW-MRI suffers from high levels of variability,[116] implying that some of the approaches presented in this paper may not work well on a patient-by-patient basis. Methodological development to improve the intrinsic quality of images should therefore go hand-by-hand with signal model development,[122] and should focus on: image quality enhancement via AI or machine learning; development of novel signal readouts that increase the robustness to motion; hardware improvements (eg, stronger field/gradient strengths), to make acquisitions faster and increase SNR.

Finally, we stress that it is not yet known how the minimum, clinically feasible DW protocol that enables resolving the microstructure exactly looks like. Research is still ongoing to understand which microstructural features can be encoded in the signal. The newest diffusion encodings, coupled with the latest estimation techniques, ever-faster acquisitions, and protocol optimization may soon increase the fidelity of DW MRI with respect to histopathology, and help us find answers to key questions such as: *How can we improve the validity of our DW-MRI models? How can we ensure generalizability across protocols and model types? Are there specific applications where one model is more suitable than another?*, as this could pave the way to personalized medicine in oncology.

Limitations

We acknowledge two main limitations in the compilation of this review.

The search was restricted using several tailored inclusion criteria. While this ensured a reproducible and complete compilation, it may have caused some articles to be left out of the selection for various reasons. For example, some methods may have only been tested in the brain (eg, pulsed and oscillating gradient MRI for assessment of cell size and extracellular space (POMACE)[123]); others may have lacked comparisons with histology[124]; and finally, some might have been missed due to variations in nomenclature, for example, a study by Iąnus et al[125] on mesorectal lymph nodes.

Lastly, we classified techniques as phenomenological or biophysical (see Fig. 3) to provide a general overview of the DW-MRI landscape. However, we acknowledge that some techniques may in fact fit both categories, for example, "partial volume" methods such as RSI or HM-MRI, here classified as biophysical.

Conclusions

Several DW-MRI techniques, including DKI, IVIM, VERDICT, IMPULSED, MDD, HM-MRI, and other have the potential to enable the noninvasive estimation of distinctive microstructural properties of cancer in the body, such as its vascularization or cellularity. These techniques provide histologically meaningful indices which, while not necessarily accurate, may still equip oncologists with useful noninvasive biomarkers. However, further research is needed before these innovative approaches can fully enter the clinic. Efforts are needed to harmonize acquisition and analysis, to strengthen inter-/intrascanner robustness, and to demonstrate histopathological validity in broader contexts.

Acknowledgments

FG receives the support of a fellowship from "la Caixa" Foundation (ID 100010434). The fellowship code is LCF/BQ/PR22/11920010. RP-L is supported by "laCaixa" Foundation, a CRIS Foundation Talent Award (TALENT 1905), the FERO Foundation, the Instituto de Salud Carlos III-Investigacion en Salud (PI18/01395 and PI21/01019), the Prostate Cancer Foundation (18YOUN19), and the Asociación Española Contra el Cáncer (AECC) (PRYCO211023SERR). AI is supported by "la Caixa" Foundation (ID 100010434) and European Union's Horizon 2020 Research and Innovation Program (Marie Skłodowska-Curie grant No. 847648), fellowship code LCF/BQ/PI20/11760029. CMWT was supported by a Veni grant (17331) from the Dutch Research Council (NWO) and a Sir Henry Wellcome Fellowship (215944/Z/19/Z). MN is supported by the Swedish Research Council (2020-04549), the Cancer Foundation (2022/2414), and ALF. This research was funded in whole, or in part, by the Wellcome Trust (Grant number 215944/Z/19/Z). For the purpose of open access, the author has applied a CC BY public copyright license to any author accepted manuscript version arising from this submission.

Conflict of Interest

MN holds stocks in Random Walk Imaging AB, which has financial interests connected to advanced diffusion encoding protocols.

References

1. Reynaud O. Time-dependent diffusion MRI in cancer: Tissue modeling and applications. Front Phys 2017;5:58.

2. Dyrby TB, Innocenti GM, Bech M, Lundell H. Validation strategies for the interpretation of microstructure imaging using diffusion MRI. Neuroimage 2018;182:62-79.

3. Stejskal EO, Tanner JE. Spin diffusion measurements: Spin echoes in the presence of a time-dependent field gradient. J Chem Phys 1965; 42(1):288. https://doi.org/10.1063/1.1695690.

4. Westin CF, Knutsson H, Pasternak O, et al. Q-space trajectory imaging for multidimensional diffusion MRI of the human brain. Neuroimage 2016;135:345-362.
5. Martinez-Heras E, Grussu F, Prados F, Solana E, Llufriu S. Diffusion-weighted imaging: Recent advances and applications. Semin Ultrasound CT MRI 2021;42(5):490-506.
6. Rokem A, Yeatman JD, Pestilli F, et al. Evaluating the accuracy of diffusion MRI models in white matter. PloS One 2015;10(4):e0123272. https://doi.org/10.1371/journal.pone.0123272.
7. Minati L, Weglarz WP. Physical foundations, models, and methods of diffusion magnetic resonance imaging of the brain: A review. Concepts Magn Reson A 2007;30A(5):278-307. https://doi.org/10.1002/cmr.a.20094.
8. Jelescu IO, Budde MD. Design and validation of diffusion MRI models of white matter. Front Phys 2017;5:61.
9. Tang L, Zhou XJ. Diffusion MRI of cancer: From low to high b-values: J Magn Reson Imaging 2019;49(1):23-40. https://doi.org/10.1002/jmri.26293
10. Brancato V, Cavaliere C, Salvatore M, Monti S. Non-Gaussian models of diffusion weighted imaging for detection and characterization of prostate cancer: A systematic review and meta-analysis. Sci Rep 2019;9(1):1-15.
11. Chatterjee A, Harmath C, Oto A. New prostate MRI techniques and sequences. Abdom Radiol 2020;45(12):4052-4062. https://doi.org/10.1007/s00261-020-02504-8.
12. Tricco AC, Lillie E, Zarin W, et al. PRISMA extension for scoping reviews (PRISMA-ScR): Checklist and explanation. Ann Intern Med 2018;169(7):467-473. https://doi.org/10.7326/M18-0850.
13. Deen SS, Priest AN, McLean MA, et al. Diffusion kurtosis MRI as a predictive biomarker of response to neoadjuvant chemotherapy in high grade serous ovarian cancer. Sci Rep 2019;9(1):10742.
14. Rosenkrantz AB, Sigmund EE, Winnick A, et al. Assessment of hepatocellular carcinoma using apparent diffusion coefficient and diffusion kurtosis indices: Preliminary experience in fresh liver explants. Magn Reson Imaging 2012;30(10):1534-1540.
15. Grussu F, Bernatowicz K, Casanova-Salas I, et al. Diffusion MRI signal cumulants and hepatocyte microstructure at fixed diffusion time: Insights from simulations, 9.4 T imaging, and histology. Magn Reson Med 2022;88(1):365-379. https://doi.org/10.1002/mrm.29174.
16. Wu G, Zhao Z, Yao Q, et al. The study of clear cell renal cell carcinoma with MR diffusion kurtosis tensor imaging and its histopathologic correlation. Acad Radiol 2018;25(4):430-438.
17. Hectors SJ, Semaan S, Song C, et al. Advanced diffusion-weighted imaging modeling for prostate cancer characterization: Correlation with quantitative histopathologic tumor tissue composition-a hypothesis-generating study. Radiology 2018;286(3):918-928.
18. Guo J, Dong C, Wu Z, et al. Diffusion kurtosis imaging assessment of the response to radiotherapy in a VX2 bone tumor model: An animal study. Acta Radiol 2022;63(2):182-191.
19. Tang WJ, Yao W, Jin Z, et al. Evaluation of the effects of anti-PD-1 therapy on triple-negative breast cancer in mice by diffusion kurtosis imaging and dynamic contrast-enhanced imaging. J Magn Reson Imaging 2022;56(6):1912-1923.
20. Xiao Z, Tang Z, Zhang J, et al. Whole-tumor histogram analysis of monoexponential and advanced diffusion-weighted imaging for sinonasal malignant tumors: Correlations with histopathologic features. J Magn Reson Imaging 2020;51(1):273-285.
21. Mori N, Inoue C, Tamura H, et al. Apparent diffusion coefficient and intravoxel incoherent motion-diffusion kurtosis model parameters in invasive breast cancer: Correlation with the histological parameters of whole-slide imaging. Magn Reson Imaging 2022;90:53-60.
22. Xiong Z, Geng Z, Lian S, et al. Discriminating rectal cancer grades using restriction spectrum imaging. Abdominal Radiology 2022;47(6):2014-2022.
23. Kiselev VG. The cumulant expansion: An overarching mathematical framework for understanding diffusion NMR. *Diffusion MRI*: Oxford University Press; Oxford, England 2010. p 152-168.
24. Jensen JH, Helpern JA, Ramani A, Lu H, Kaczynski K. Diffusional kurtosis imaging: The quantification of non-gaussian water diffusion by means of magnetic resonance imaging. Magn Reson Med 2005;53(6):1432-1440. https://doi.org/10.1002/mrm.20508.
25. Szczepankiewicz F, van Westen D, Englund E, et al. The link between diffusion MRI and tumor heterogeneity: Mapping cell eccentricity and density by diffusional variance decomposition (DIVIDE). Neuroimage 2016;142:522-532.
26. Fang S, Yang Y, Chen B, et al. DWI and IVIM imaging in a murine model of rhabdomyosarcoma: Correlations with quantitative histopathologic features. J Magn Reson Imaging 2022;55(1):225-233. https://doi.org/10.1002/jmri.27828.
27. Yuan Q, Kapur P, Zhang Y, et al. Intratumor heterogeneity of perfusion and diffusion in clear-cell renal cell carcinoma: Correlation with tumor cellularity. Clin Genitourin Cancer 2016;14(6):e585-e594.
28. Yin Y, Sedlaczek O, Muller B, et al. Tumor cell load and heterogeneity estimation from diffusion-weighted MRI calibrated with histological data: An example from lung cancer. IEEE Trans Med Imaging 2018;37(1):35-46.
29. Meyer HJ, Hohn AK, Woidacki K, et al. Associations between IVIM histogram parameters and histopathology in rectal cancer. Magn Reson Imaging 2021;4(77):21-27.
30. Hecht EM, Liu MZ, Prince MR, et al. Can diffusion-weighted imaging serve as a biomarker of fibrosis in pancreatic adenocarcinoma? J Magn Reson Imaging 2017;46(2):393-402.
31. Winfield JM, Miah AB, Strauss D, et al. Utility of multi-parametric quantitative magnetic resonance imaging for characterization and radiotherapy response assessment in soft-tissue sarcomas and correlation with histopathology. Front Oncol 2019;9:280.
32. Cai SQ, Li Y, Li YA, et al. Perfusion-based functional magnetic resonance imaging for differentiating serous borderline ovarian tumors from early serous ovarian cancers in a rat model. Acta Radiol 2021;62(1):129-138.
33. Wu H, Liu H, Liang C, et al. Diffusion-weighted multiparametric MRI for monitoring longitudinal changes of parameters in rabbit VX2 liver tumors. J Magn Reson Imaging 2016;44(3):707-714.
34. Liu Q, Zhang J, Jiang M, et al. Evaluating the histopathology of pancreatic ductal adenocarcinoma by intravoxel incoherent motion-diffusion weighted imaging comparing with diffusion weighted imaging. Front Oncol 2021;11:670085.
35. Song XL, Kang HK, Jeong GW, et al. Intravoxel incoherent motion diffusion-weighted imaging for monitoring chemotherapeutic efficacy in gastric cancer. World J Gastroenterol 2016;22(24):5520.
36. Lee HJ, Rha SY, Chung YE, et al. Tumor perfusion-related parameter of diffusionweighted magnetic resonance imaging: Correlation with histological microvessel density. Magn Reson Med 2014;71(4):1554-1558.
37. Mayer P, Fritz F, Koell M, et al. Assessment of tissue perfusion of pancreatic cancer as potential imaging biomarker by means of intravoxel incoherent motion MRI and CT perfusion: Correlation with histological microvessel density as ground truth. Cancer Imaging 2021;21(1):13.
38. Li JL, Ye WT, Liu ZY, et al. Comparison of microvascular perfusion evaluation among IVIM-DWI, CT perfusion imaging and histological microvessel density in rabbit liver VX2 tumors. Magn Reson Imaging 2018;46:64-69.
39. Yang SH, Lin J, Lu F, et al. Evaluation of antiangiogenic and antiproliferative effects of sorafenib by sequential histology and intravoxel incoherent motion diffusion-weighted imaging in an orthotopic hepatocellular carcinoma xenograft model. J Magn Reson Imaging 2017;45(1):270-280.
40. Hompland T, Hole KHK, Ragnum HB, et al. Combined MR imaging of oxygen consumption and supply reveals tumor hypoxia and

aggressiveness in prostate cancer patients. Cancer Res 2018;78(16): 4774-4785.

41. Tao J, Yin Z, Li X, et al. Correlation between IVIM parameters and microvessel architecture: Direct comparison of MRI images and pathological slices in an orthotopic murine model of rhabdomyosarcoma. Eur Radiol 2023; 33:8576–8584.

42. Zhang Z, Shen S, Ma J, et al. Sequential multi-parametric MRI in assessment of the histological subtype and features in the malignant pleural mesothelioma xenografts. Heliyon 2023;9(4):e15237.

43. Xie S, Qiu C, Sun Y, et al. Series of intravoxel incoherent motion and T2* magnetic resonance imaging mapping in detection of liver perfusion changes and regeneration among partial hepatectomy in Sprague–Dawley rats. Acad Radiol 2022;29(12):1810-1818.

44. Le Bihan D, Breton E, Lallemand D, Grenier P, Cabanis E, Laval-Jeantet M. MR imaging of intravoxel incoherent motions: Application to diffusion and perfusion in neurologic disorders. Radiology 1986; 161(2):401-407.

45. Jerome NP, D'Arcy JA, Feiweier T, et al. Extended T2-IVIM model for correction of TE dependence of pseudo-diffusion volume fraction in clinical diffusion-weighted magnetic resonance imaging. Phys Med Biol 2016;61(24):N667-N680.

46. Liu Y, Wang X, Cui Y, et al. Comparative study of monoexponential, intravoxel incoherent motion, kurtosis, and IVIM-kurtosis models for the diagnosis and aggressiveness assessment of prostate cancer. Front Oncol 2020;9(10):1763.

47. Barbieri S, Donati OF, Froehlich JM, Thoeny HC. Impact of the calculation algorithm on biexponential fitting of diffusion-weighted MRI in upper abdominal organs. Magn Reson Med 2016;75(5):2175-2184.

48. Lasic S, Nilsson M, Latt J, Stahlberg F, Topgaard D. Apparent exchange rate mapping with diffusion MRI. Magn Reson Med 2011; 66(2):356-365.

49. Wetscherek A, Stieltjes B, Laun FB. Flow-compensated intravoxel incoherent motion diffusion imaging. Magn Reson Med 2015;74(2): 410-419.

50. Ahlgren A, Knutsson L, Wirestam R, et al. Quantification of microcirculatory parameters by joint analysis of flow-compensated and non-flow-compensated intravoxel incoherent motion (IVIM) data. NMR Biomed 2016;29(5):640-649.

51. Sijtsema ND, Petit SF, Poot DH, et al. An optimal acquisition and post-processing pipeline for hybrid IVIM-DKI in head and neck. Magn Reson Med 2021;85(2):777-789.

52. Bonet-Carne E, Johnston E, Daducci A, et al. VERDICT-AMICO: Ultrafast fitting algorithm for non-invasive prostate microstructure characterization. NMR Biomed 2019;32(1):e4019.

53. Bailey C, Bourne RM, Siow B, et al. VERDICT MRI validation in fresh and fixed prostate specimens using patient-specific moulds for histological and MR alignment. NMR Biomed 2019;32(5):e4073.

54. Duchene G, Abarca-Quinones J, Leclercq I, Duprez T, Peeters F. Insights into tissue microstructure using a double diffusion encoding sequence on a clinical scanner: Validation and application to experimental tumor models. Magn Reson Med 2020;83(4):1263-1276.

55. Panagiotaki E, Walker-Samuel S, Siow B, et al. Noninvasive quantification of solid tumor microstructure using VERDICT MRI. Cancer Res 2014;74(7):1902-1912.

56. Johnston EW, Bonet-Carne E, Ferizi U, et al. VERDICT MRI for prostate cancer: Intracellular volume fraction versus apparent diffusion coefficient. Radiology 2019;291(2):391-397. https://doi.org/10.1148/radiol.2019181749.

57. Bailey C, Collins DJ, Tunariu N, et al. Microstructure characterization of bone metastases from prostate cancer with diffusion MRI: Preliminary findings. Front Oncol 2018;8:26.

58. Johnston E, Pye H, Bonet-Carne E, et al. INNOVATE: A prospective cohort study combining serum and urinary biomarkers with novel diffusion-weighted magnetic resonance imaging for the prediction and characterization of prostate cancer. BMC Cancer 2016;16(1):816.

59. Palombo M, Valindria V, Singh S, et al. Joint estimation of relaxation and diffusion tissue parameters for prostate cancer with relaxation-VERDICT MRI. Sci Rep 2023;13(1):1-13.

60. Panagiotaki E, Chan RW, Dikaios N, et al. Microstructural characterization of normal and malignant human prostate tissue with vascular, extracellular, and restricted diffusion for cytometry in tumours magnetic resonance imaging. Invest Radiol 2015;50(4):218-227.

61. Panagiotaki E, Schneider T, Siow B, Hall MG, Lythgoe MF, Alexander DC. Compartment models of the diffusion MR signal in brain white matter: A taxonomy and comparison. Neuroimage 2012; 59(3):2241-2254.

62. Chiou E, Valindria V, Giganti F, Punwani S, Kokkinos I, Panagiotaki E. Synthesizing VERDICT maps from standard DWI data using GANs. Lecture Notes in Computer Science (including subseries Lecture Notes in Artificial Intelligence and Lecture Notes in Bioinformatics); 2021, 13006 LNCS, pp. 58–67. Available from: https://link.springer.com/chapter/10.1007/978-3-030-87615-9_6

63. Jiang X, Xu J, Gore JC. Mapping hepatocyte size in vivo using temporal diffusion spectroscopy MRI. Magn Reson Med 2020;84(5):2671-2683.

64. Xu J, Jiang X, Li H, et al. Magnetic resonance imaging of mean cell size in human breast tumors. Magn Reson Med 2020;83(6):2002-2014.

65. Jiang X, Dudzinski S, Beckermann KE, et al. MRI of tumor T cell infiltration in response to checkpoint inhibitor therapy. J Immunother Cancer 2020;8(1):e000328.

66. Jiang X, Li H, Xie J, et al. In vivo imaging of cancer cell size and cellularity using temporal diffusion spectroscopy. Magn Reson Med 2017; 78(1):156-164.

67. Li H, Jiang X, Xie J, Gore JC, Xu J. Impact of transcytolemmal water exchange on estimates of tissue microstructural properties derived from diffusion MRI. Magn Reson Med 2017;77(6):2239.

68. Wu D, Jiang K, Li H, et al. Time-dependent diffusion MRI for quantitative microstructural mapping of prostate cancer. Radiology 2022; 303(3):578-587.

69. Jiang X, Devan SP, Xie J, Gore JC, Xu J. Improving MR cell size imaging by inclusion of transcytolemmal water exchange. NMR Biomed 2022;35(12):e4799.

70. Bennett KM, Schmainda KM, Bennett R, Rowe DB, Lu H, Hyde JS. Characterization of continuously distributed cortical water diffusion rates with a stretched-exponential model. Magn Reson Med 2003; 50(4):727-734.

71. Senn N, Masannat Y, Husain E, Siow B, Heys SD, He J. q-Space imaging yields a higher effect gradient to assess cellularity than conventional diffusion-weighted imaging methods at 3.0 T: A pilot study with freshly excised whole-breast tumors. Radiol Imaging Cancer 2019;1(1): e190008.

72. Novikov DS, Fieremans E, Jespersen SN, Kiselev VG. Quantifying brain microstructure with diffusion MRI: Theory and parameter estimation. NMR Biomed 2019;32(4):e3998. https://doi.org/10.1002/nbm.3998.

73. Yamada I, Hikishima K, Miyasaka N, et al. Esophageal carcinoma: Evaluation with q-space diffusion-weighted MR imaging ex vivo. Magn Reson Med 2015;73(6):2262-2273.

74. Callaghan PT, Eccles CD, Xia Y. NMR microscopy of dynamic displacements: k-space and q-space imaging. J Phys E: Sci Instr 1988; 21(8):820. https://doi.org/10.1088/0022-3735/21/8/017/meta.

75. Latt J, Nilsson M, Malmborg C, et al. Accuracy of q-space related parameters in MRI: Simulations and phantom measurements. IEEE Trans Med Imaging 2007;26(11):1437-1447.

76. Ozarslan E, Koay CG, Shepherd TM, et al. Mean apparent propagator (MAP) MRI: A novel diffusion imaging method for mapping tissue microstructure. Neuroimage 2013;9(78):16.

77. Wedeen VJ, Hagmann P, Tseng WYI, Reese TG, Weisskoff RM. Mapping complex tissue architecture with diffusion spectrum magnetic resonance imaging. Magn Reson Med 2005;54(6):1377-1386. https://doi.org/10.1002/mrm.20642.

78. Xu J, Jiang X, Devan SP, et al. MRI-cytometry: Mapping non-parametric cell size distributions using diffusion MRI. Magn Reson Med 2021;85(2):748.

79. Yamin G, Schenker-Ahmed NM, Shabaik A, et al. Voxel level radiologic pathologic validation of restriction spectrum imaging cellularity index with Gleason grade in prostate cancer. Clin Cancer Res 2016; 22(11):2668-2674.

80. White NS, Leergaard TB, D'Arceuil H, Bjaalie JG, Dale AM. Probing tissue microstructure with restriction spectrum imaging: Histological and theoretical validation. Hum Brain Mapp 2013;34(2):327-346.

81. Morelli L, Palombo M, Buizza G, et al. Microstructural parameters from DW-MRI for tumour characterization and local recurrence prediction in particle therapy of skull-base chordoma. Med Phys 2023;50(5):2900-2913.

82. Nilsson M, Alerstam E, Wirestam R, et al. Evaluating the accuracy and precision of a two-compartment Karger model using Monte Carlo simulations. J Magn Reson 2010;206(1):59-67.

83. Topgaard D. Isotropic diffusion weighting in PGSE NMR: Numerical optimization of the q-MAS PGSE sequence. Micropor Mesopor Mater 2013;9(178):60-63.

84. Eriksson S, Lasic S, Topgaard D. Isotropic diffusion weighting in PGSE NMR by magic-angle spinning of the q-vector. J Magn Reson 2013; 1(226):13-18.

85. Naranjo ID, Reymbaut A, Brynolfsson P, et al. Multidimensional diffusion magnetic resonance imaging for characterization of tissue microstructure in breast cancer patients: A prospective pilot study. Cancers (Basel) 2021;13(7):1606.

86. Nilsson M, Eklund G, Szczepankiewicz F, et al. Mapping prostatic microscopic anisotropy using linear and spherical b-tensor encoding: A preliminary study. Magn Reson Med 2021;86(4):2025-2033.

87. Langbein BJ, Szczepankiewicz F, Westin CF, et al. A pilot study of multidimensional diffusion MRI for assessment of tissue heterogeneity in prostate cancer. Invest Radiol 2021;56(12):845-853.

88. Topgaard D. Multidimensional diffusion MRI. J Magn Reson 2017; 2(275):98-113.

89. Topgaard D. Diffusion tensor distribution imaging. NMR Biomed 2019;32(5):e4066.

90. Szczepankiewicz F, Sjolund J, Stahlberg F, Latt J, Nilsson M. Tensor-valued diffusion encoding for diffusional variance decomposition (DIVIDE): Technical feasibility in clinical MRI systems. PloS One 2019; 14(3):e0214238.

91. Chatterjee A, Mercado C, Bourne RM, et al. Validation of prostate tissue composition by using hybrid multidimensional MRI: Correlation with histologic findings. Radiology 2022;302(2):368-377. https://doi.org/10.1148/radiol.2021204459.

92. Chatterjee A, Antic T, Gallan AJ, et al. Histological validation of prostate tissue composition measurement using hybrid multi-dimensional MRI: Agreement with pathologists' measures. Abdominal Radiology 2022;47(2):801-813.

93. Chatterjee A, Bourne RM, Wang S, et al. Diagnosis of prostate cancer with noninvasive estimation of prostate tissue composition by using hybrid multidimensional MR imaging: A feasibility study. Radiology 2018;287(3):863-873.

94. Slator PJ, Palombo M, Miller KL, et al. Combined diffusion-relaxometry microstructure imaging: Current status and future prospects. Magn Reson Med 2021;86(6):2987.

95. Lemberskiy G, Fieremans E, Veraart J, Deng FM, Rosenkrantz AB, Novikov DS. Characterization of prostate microstructure using water diffusion and NMR relaxation. Front Phys 2018;6:91.

96. Kim D, Doyle EK, Wisnowski JL, Kim JH, Haldar JP. Diffusion-relaxation correlation spectroscopic imaging (DR-CSI): A multi-dimensional approach for probing microstructure. Magn Reson Med 2017;78(6):2236.

97. De Almeida Martins JP, Topgaard D. Multidimensional correlation of nuclear relaxation rates and diffusion tensors for model-free investigations of heterogeneous anisotropic porous materials. Sci Rep 2018;8(1):1-12.

98. Hurlimann M, Venkataramanan L, Flaum C. The diffusion–spin relaxation time distribution function as an experimental probe to characterize fluid mixtures in porous media. J Chem Phys 2002; 117(22):10223-10232.

99. Zhang Z, Wu HH, Priester A, et al. Prostate microstructure in prostate cancer using 3-T MRI with diffusion-relaxation correlation spectrum imaging: Validation with whole mount digital histopathology. Radiology 2020;296(2):348-355.

100. Dai Y, Hu W, Wu G, et al. Grading clear cell renal cell carcinoma grade using diffusion relaxation correlated MR spectroscopic imaging. J Magn Reson Imaging 2023. https://doi.org/10.1002/jmri.28777

101. Sun Y, Reynolds HM, Wraith D, et al. Voxel-wise prostate cell density prediction using multiparametric magnetic resonance imaging and machine learning. Acta Oncol 2018;57(11):1540-1546.

102. De Perrot T, Sadjo Zoua C, Glessgen CG, et al. Diffusion-weighted MRI in the genitourinary system. J Clin Med 2022;11(7):1921.

103. De Cataldo C, Bruno F, Palumbo P, et al. Apparent diffusion coefficient magnetic resonance imaging (ADC-MRI) in the axillary breast cancer lymph node metastasis detection: A narrative review. Gland Surg 2020;9(6):2225.

104. Vollenbrock SE, Voncken FE, Bartels LW, Beets-Tan RG, Bartels-Rutten A. Diffusion-weighted MRI with ADC mapping for response prediction and assessment of oesophageal cancer: A systematic review. Radiother Oncol 2020;142:17-26.

105. Turkbey B, Rosenkrantz AB, Haider MA, et al. Prostate imaging reporting and data system version 2.1: 2019 update of prostate imaging reporting and data system version 2. Eur Urol 2019;76(3):340-351.

106. Surov A, Meyer HJ, Wienke A. Correlations between apparent diffusion coefficient and Gleason score in prostate cancer: A systematic review. Eur Urol Oncol 2020;3(4):489-497.

107. Manetta R, Palumbo P, Gianneramo C, et al. Correlation between ADC values and Gleason score in evaluation of prostate cancer: Multicentre experience and review of the literature. Gland Surg 2019;8 (Suppl 3):S216.

108. Chen L, Liu M, Bao J, et al. The correlation between apparent diffusion coefficient and tumor cellularity in patients: A meta-analysis. PloS One 2013;8(11):e79008.

109. Brabec J, Friedjungova M, Vásata D, et al. Meningioma microstructure assessed by diffusion MRI: An investigation of the source of mean diffusivity and fractional anisotropy by quantitative histology. NeuroImage Clin 2023;37:103365.

110. Surov A, Eger KI, Potratz J, Gottschling S, Wienke A, Jechorek D. Apparent diffusion coefficient correlates with different histopathological features in several intrahepatic tumors. Eur Radiol 2023;33(9):5955-5964.

111. Petralia G, Koh DM, Attariwala R, et al. Oncologically relevant findings reporting and data system (ONCO-RADS): Guidelines for the acquisition, interpretation, and reporting of whole-body MRI for cancer screening. Radiology 2021;299(3):494-507.

112. Ljimani A, Caroli A, Laustsen C, et al. Consensus-based technical recommendations for clinical translation of renal diffusion-weighted MRI. Magn Reson Mater Phys Biol Med 2020;33:177-195.

113. Baltzer P, Mann RM, Iima M, et al. Diffusion-weighted imaging of the breast—A consensus and mission statement from the EUSOBI international breast diffusion-weighted imaging working group. Eur Radiol 2020;30:1436-1450.

114. Jelescu IO, Veraart J, Fieremans E, Novikov DS. Degeneracy in model parameter estimation for multicompartmental diffusion in neuronal tissue. NMR Biomed 2016;29(1):33-47.

115. Lampinen B, Szczepankiewicz F, Latt J, et al. Probing brain tissue microstructure with MRI: Principles, challenges, and the role of multidimensional diffusionrelaxation encoding. Neuroimage 2023;282: 120338.

116. Barbieri S, Gurney-Champion OJ, Klaassen R, Thoeny HC. Deep learning how to fit an intravoxel incoherent motion model to diffusion-weighted MRI. Magn Reson Med 2020;83(1):312-321. https://doi.org/10.1002/mrm.27910.

117. de Almeida Martins JP, Nilsson M, Lampinen B, et al. Neural networks for parameter estimation in microstructural MRI: Application to a diffusion-relaxation model of white matter. Neuroimage 2021;12(244):118601.

118. Bourne RM, Bailey C, Johnston EW, et al. Apparatus for histological validation of in vivo and ex vivo magnetic resonance imaging of the human prostate. Front Oncol 2017;7:47.

119. Szczepankiewicz F, Lasic S, van Westen D, et al. Quantification of microscopic diffusion anisotropy disentangles effects of orientation dispersion from microstructure: Applications in healthy volunteers and in brain tumors. Neuroimage 2015;104:241-252.

120. Nilsson M, Lasic S, Drobnjak I, Topgaard D, Westin CF. Resolution limit of cylinder diameter estimation by diffusion MRI: The impact of gradient waveform and orientation dispersion. NMR Biomed 2017; 30(7):e3711.

121. Tax CM, Grussu F, Kaden E, et al. Cross-scanner and cross-protocol diffusion MRI data harmonisation: A benchmark database and evaluation of algorithms. Neuroimage 2019;7(195):285-299.

122. Tax CM, Bastiani M, Veraart J, Garyfallidis E, Irfanoglu MO. What's new and what's next in diffusion MRI preprocessing. Neuroimage 2022;249:118830.

123. Reynaud O, Winters KV, Hoang DM, Wadghiri YZ, Novikov DS, Kim SG. Pulsed and oscillating gradient MRI for assessment of cell size and extracellular space (POMACE) in mouse gliomas. NMR Biomed 2016;29(10):1350-1363.

124. Xing S, Levesque IR. A simulation study of cell size and volume fraction mapping for tissue with two underlying cell populations using diffusion-weighted MRI. Magn Reson Med 2021;86(2):1029-1044.

125. Ianus A, Santiago I, Galzerano A, et al. Higher-order diffusion MRI characterization of mesorectal lymph nodes in rectal cancer. Magn Reson Med 2020;84(1):348-364.

Appendix A

Diffusion MRI Physics Fundamentals

This appendix presents the physical fundamentals of diffusion MRI, providing context to the literature review. In the following, the terms *water molecules*, *protons*, and *spins* will be used interchangeably to refer to the motion of them.

A.1. Diffusion Encoding

Time-varying magnetic field gradients are used to sensitize the MRI signal to diffusion. The classical DW-MRI experiment is based on the pulsed-gradient spin-echo (PGSE) approach, also known as the Stejskal-Tanner experiment, single diffusion encoding, or, more recently, as linear b-tensor encoding. The schematic of a PGSE sequence is shown in Fig. 1.

The PGSE approach is based on the spin echo experiment, in which two radiofrequency (RF) pulses, of flip angle 90° and 180°, separated by a time TE/2 are used to irradiate the sample. The first pulse excites the tissue, creating a component of magnetization orthogonal to the static field. The second pulse refocuses the magnetization by cancelling out the effect of field inhomogeneities. The signal is sampled at a time TE, that is, when the refocusing is complete, and the signal is weighted by the underlying T2 relaxation constant, that is, proportional to $e^{-\frac{TE}{T2}}$. In PGSE, two magnetic field gradient lobes (known as diffusion-encoding gradients) are added on either side of the refocusing pulse. The first gradient lobe effectively tags water molecule's phases depending on their spatial position, so that their phases will now depend on their position along the gradient direction. Conversely, the effect of the combination of the refocusing pulse and of the second gradient lobe is that of cancelling out the phase distribution modulation caused by the previous lobe, for those molecules that do not move. If all spins were perfectly static during diffusion-encoding, one would measure the same T2-weighted signal that one would have obtained without diffusion encoding. However, due to diffusion, water molecules change their position in between the two gradient lobes, as well as during the application of each lobe itself. This implies that a full phase coherence over the spin ensemble will not be re-established at the echo time $t = \mathrm{TE}$, so that the signal measured will be smaller than the one obtained without diffusion-weighting, leading to signal attenuation. The amount of attenuation increases as the degree of diffusion taking place increases, resulting in DW images of lower intensity. b-value and diffusion time.

The amount of signal loss caused by diffusion-weighting depends on several factors. Some depend on the tissue being imaged, such as the underlying intrinsic diffusion coefficient and the characteristics of the microstructure, for example, type and features of the biological structures that restrict or hinder diffusion. These features include, for example, the density and size of cells. Other factors depend instead on the acquisition, and are: the gradient magnitude G, the gradient duration δ, and the gradient separation Δ (see Fig. 1). The total DW-signal S is the ensemble average of the signals from all spins, that is,

$$S = S_0 < e^{i\phi} > \tag{16}$$

where S_0 is the T2-weighted, non-DW-reference signal and ϕ is the phase accrued by a generic spin. ϕ depends on the interaction between a spin's random walk over time $\mathbf{r}(t)$ and the temporal evolution of the diffusion encoding gradient $\mathbf{g}(t)$, that is,

$$\phi = -\gamma \int_0^{TE} \mathbf{g}(t) \cdot \mathbf{r}(t) dt \tag{17}$$

For free water self-diffusion without any barriers, Eq. 16 simplifies to

$$S = S_0 \exp(-b\, D_{\mathrm{water}}) \tag{18}$$

Above, S_0 is the non-DW signal (proton density-, T2-, and potentially T1-weighted), whereas D_{water} is the intrinsic diffusivity of water at the experiment temperature, and b provides a general indication of the overall strength of the

diffusion-weighting. This factor depends on the acquisition settings, and is routinely known as *b*-value. It can be calculated as:

$$b = \gamma^2 G^2 \delta^2 (\Delta - \delta/3) \tag{19}$$

where γ is the proton gyromagnetic ratio, and G, δ, and Δ the gradient parameters. Another useful sequence parameter is the overall diffusion time $t_{\text{diff}} = \Delta - \delta/3$. This provides an indication of the amount of time that diffusing water molecules are allowed to experience the microstructure, before the MRI signal is acquired.

A.2. Intravoxel Heterogeneity Mapping With PGSE

The voxel size of in vivo MRI in humans is of the order of a few cube millimeters. The observed MR-signal in a voxel arises from contributions of various diffusion processes taking place within different cellular components, since the voxel size is much larger than the scale of the microstructure where diffusion takes place ($\sim 1 - 100$ µm). As a consequence, in vivo DW-MRI measurements are characterized by intrinsic, intravoxel partial volume effects, and the signal entangles the contribution of multiple water pools in one measurement. Different techniques have been proposed to disentangle such contributions, with the ultimate aim of obtaining sensitive and specific biomarkers of tissue microstructure. The solutions proposed in the literature span phenomenological signal representations (eg, estimation of apparent diffusion and kurtosis coefficients, stretched exponential, anomalous diffusion), multicompartment biophysical models, and include recent approaches based on innovative diffusion acquisitions such as double diffusion encoding and *b*-tensor encoding.[4,86]

The section below provides a general overview of the techniques available for microstructure inference in DW-MRI. The section aims to provide some context for the detailed description of the methods found in our systematic literature search. Importantly, we point out that the inference of microstructure from signal measurements is a challenging task: different combinations of microstructural parameters can provide virtually indistinguishable signals in certain measurement regimes and in the presence of noise, making microstructure estimation an ill-posed inverse problem.[114]

A.2.1. PHENOMENOLOGICAL SIGNAL REPRESENTATIONS.

It can be shown that the signal in Eq. (16) can be expanded as a function of increasing powers of the *b*-value, that is, $\ln(S) \sim \sum_{k=1} a_k b^k$ (the cumulant expansion[23]), where coefficients *ak* are related to the cumulants of the spin displacement distribution within a voxel. Expanding Eq. (16) up to the second power of b (that is, with an approximation error proportional to $O(b^3)$), provides

$$S = S = S_0 \exp\left(-b\,\text{ADC} + \frac{1}{6} K (b\,\text{ADC})^2\right) \tag{20}$$

In Eq. (20) above, ADC and K are, respectively, the apparent diffusion and excess kurtosis coefficients along the direction of the diffusion encoding gradient. ADC provides a measurement of the overall amount of diffusion taking place during the measurement along the gradient direction, so that higher ADC implies stronger signal decay. Conversely, K gives an indication of how much the diffusion process departs from Gaussian, free diffusion. While $K = 0$ would imply perfectly Gaussian diffusion, that is, mono-exponential signal decay, a nonzero K can arise when 1) multiple Gaussian water pools with different intrinsic diffusivities are found inside the same voxel, 2) diffusion is restricted by geometric confinements, 3) orientation dispersion of microscopic domains exists within the voxel, 4) different water compartment exchange water during the MRI signal encoding, or by a combination of all of these. Signal representations as those in Eq. (20) are sometimes referred to as *phenomenological*: they provide a description of the signal and link this to the statistical moments of the spin displacement distribution, but without seeking to estimate the biophysical *causes* of the observed diffusion phenomenon (eg, without trying to estimate biophysical properties such as cell size, cell density, etc). On the one hand, phenomenological representations do not make any assumptions on the geometry of the tissue (eg, modeling cells as spheres[60]). On the other hand, measures such as ADC or K may be difficult to interpret, being surrogate indices that entail contributions from multiple biological factors in one number.

When the *b*-value is not too high (generally, not exceeding 400–800 seconds/mm^2 in body imaging or 1000–1500 seconds/mm^2 in the brain), the first-order term in the *b*-value (cumulant) expansion is dominant, and the expansion reduces to

$$S = S_0\, e^{-b\,\text{ADC}} \tag{21}$$

where S_0 is the non-DW-signal, b the *b*-value and ADC is the apparent diffusion coefficient. ADC is a sensitive marker of tissue microstructure, but has relatively poor biological specificity, since contributions from different water compartments within the same voxel (eg, intra-/extracellular water) are pooled together in one, average number. This implies that ADC measurements do not describe the complicated diffusion process in heterogeneous microstructures accurately: signal contributions from different processes within a voxel, including pseudo-diffusion due to perfusion, are integrated and modeled by one single diffusion coefficient, which also depends on the particular diffusion times used for the acquisition (eg, gradient duration δ and gradient separation Δ). Due to this, the ADC is defined as an "apparent" coefficient. Nonetheless, ADC is easy to obtain (ADC maps can be computed with as few as two images), and offers sensitivity to

alterations in tissue microstructure due to pathology, classification or grading of tumors, and therapy response assessment.

A.2.2. MULTI-COMPARTMENT BIOPHYSICAL MODELING. Multi-compartment biophysical models describe the DW-signal as arising from the contribution of multiple water pools located in different cellular compartments, as for example intracellular or extracellular water. Fitting such models to sets of DW measurements may provide voxel-wise estimates of salient biophysical properties, as for example intracellular water fraction or characteristic restriction size, effectively reflecting intravoxel cell size statistics.

The number and characteristics of the tissue parameters that can be estimated depends on the assumptions made when building the geometric representation of the biophysical model—for example, spherical vs. elongated cells, characteristics of the cell size distribution, etc— as well as on the acquisition protocol. The most common tissue parameters that are estimated in biophysical modeling are:

- compartment-wise signal fractions, for example, f_{vasc}, f_{ic}, or f_{EES}, which, respectively, represent the fraction of signal coming from vascular water, intracellular water and extracellular extravascular water;
- cell size radius R or diameter d in μm;
- cellularity indices C, that is, with units in cells/mm^2 or cells/mm^3. A common way of estimating C is to combine metrics such as f_{ic} and d in one number, for example, $C \propto \frac{f_{ic}}{d^3}$.[55]

A.3. Other Approaches Beyond PGSE

PGSE is the most common diffusion MRI acquisition implementation, and is available in virtually all clinical scanners. However, several other implementations of the DW-MRI experiment exist. Some of the latest implementations probe new diffusion contrasts that are not physically accessible with standard PGSE, and therefore offer great promise for the development of new biomarkers of cancer. Nevertheless, these more advanced implementations often come at a price, as for example the need for strong gradient systems, longer echo times TE, and may not yet be available as vendor-provided implementations on clinical systems.

Oscillating gradient spin echo (OGSE) is similar to PGSE, in that two diffusion gradient wave forms are inserted on either side of the refocusing pulse of a spin echo sequence. However, in OGSE, the gradient is not pulsed, but it is rather made of an oscillating waveform at a specific frequency f.[123] A key characteristic of OGSE is that it enables probing much shorter effective diffusion times t_{diff} than PGSE, at a given b-value.

Double-diffusion encoding (DDE) combines in one acquisition two diffusion encoding blocks, separated by a mixing time.[54] The two diffusion encoding gradients are consecutively applied with two different orientations, separated by a relative angle ψ. DDE enables probing diffusion correlations, resolving properties of microscopic domains (eg, anisotropy and/or eccentricity of pores where restricted diffusion takes place) without the confounding effect of the macroscopic, orientational arrangement of the ensemble of the microscopic domains.

DDE also finds application in filter-exchange imaging (FEXI).[48] In FEXI, a first diffusion encoding block acts as a filter that suppresses the signal from fast diffusing components. The signal read at the end of the second block will be modulated by the amount of water exchange between water compartments taking place during the mixing time. FEXI has been used to measure the apparent exchange rate (sensitive to cell membrane permeability, but it is not a measure of permeability as such) and other exchange processes, as for example in breast cancer.[48]

Multidimensional diffusion (MDD) MRI is an innovative diffusion MRI framework that relies on a new diffusion encoding paradigm (also known as b-tensor encoding, or q-space trajectory imaging).[4,83,84,88] MDD generalizes the traditional approach based on PGSE (which is, in fact, a special case of b-tensor diffusion gradient), sensitizing the measurements to different diffusion directions at once and thus probing new diffusion contrasts that are not accessible to standard PGSE.

Appendix B

Search Query

("cellsize*"[tiab]OR"intra-cellularfraction*"[tiab]ORcellularity [tiab]ORcytometry[tiab]OR"CellSize"[Mesh]

OR "cell density"[tiab] OR "volume fraction*" OR "component fraction*"[tiab] OR "perfusion fraction*"[tiab] OR "vascular fraction*"[tiab] OR "fractional volume*"[tiab] OR "tissue component*"[tiab] OR "tissue composition*"[tiab])

AND (histolog*[tiab] OR histologic[tiab] or histologically[tiab] OR histology[tiab] OR histopatholog*[tiab] OR patholog*[tiab] OR microstructur*[tiab])

AND (oncology[tiab] OR tumor[tiab] OR tumour[tiab] OR abdominal[tiab] OR liver[tiab] OR pelvic[tiab] OR hepato*[tiab] OR musc*[tiab] OR cancer[tiab] OR prostate*[tiab])

AND ("DW-MRI"[tiab] OR "diffusion MRI"[tiab] OR "dMRI"[tiab] OR "diffusion weighted imaging"[tiab] OR "DWI"[tiab] OR "Diffusion Magnetic Resonance Imaging"[tiab] OR "Diffusion Magnetic Resonance Imaging"[Mesh] OR "Diffusion-relaxometry"[tiab] OR "Diffusion Relaxometry"[tiab] OR DWI[tiab] OR "multi-dimensional MRI"[tiab] OR "multiparametric MRI"[tiab] OR mpMRI[tiab] OR bpMRI[tiab] OR mp-MRI[tiab] OR "multi-parametric MRI"[tiab])

AND (estimat*[tiab] OR predict*[tiab] OR correlat*[tiab] OR validat*[tiab])

NOT (neuro*[tiab] OR cerebral*[tiab] OR "Neurology"[Mesh] OR "Brain"[Mesh] OR brain[tiab])

Appendix C

Fitting Algorithms

TABLE C1. Different Fitting Algorithms That Can Be Used to Fit the IVIM-Model to Measure DW-MR Signal Data[47,116]

Algorithm	Type	Estimated Parameters	Method Description
Levenberg–Marquardt (LM)	Least-squares	D_p, f, D^*	• Determines values of the three parameters simultaneously in each voxel • No boundary constraints possible
Trust region (TR) based	Least-squares	D_p, f, D^*	• Determines values of the three parameters simultaneously in each voxel
			• Uses restricted search space, boundary constraints easily incorporated
Fixed D^*	Least-squares	f, D_t	• Same as TR, but now with D^* fixed to a value defined a priori
Segmented unconstrained (SU)	Multi-step	In first step: D_t and f	• Most frequently used algorithm for IVIM analysis
		In second step: D^*	• Uses assumption that D_t is dominant at high b-values and that D^* is negligible here • Uses TR based algorithm in the second step
Segmented constrained (SC)	Multi-step	In first step: D_t and f	• Similar to SU
		In second step: D^*	• Now assumes that the intercept of S is equal to S_0
Bayesian probability (BP)	BP-based	D_p, f, D^*	• Does not fit each voxel independently • Fits using a kind of spatial similarity additional information incorporated
Deep neural network (DNN)	Auto-encoder	D_p, f, D^*	• Unsupervised network with three hidden layers
			• Constraint: the input signal should be encoded by the three IVIM parameters • Increased fitting speed in comparison with LM and BP algorithms

The algorithm that is used the most for both IVIM fitting and VERDICT fitting is LM.